

Comparisons of fresh complex impact craters on Mercury and the Moon: Implications for controlling factors in impact excavation processes

Zhiyong Xiao ^{a,b,*}, Robert G. Strom ^b, Clark R. Chapman ^c, James W. Head ^d, Christian Klimczak ^e, Lillian R. Ostrach ^f, Jörn Helbert ^g, Piero D'Incecco ^g

^a Planetary Science Institute, Faculty of Earth Sciences, China University of Geosciences (Wuhan), Wuhan, Hubei 430074, China

^b Lunar and Planetary Laboratory, University of Arizona, Tucson, AZ 85719, USA

^c Department of Space Studies, Southwest Research Institute, Boulder, CO 80302, USA

^d Department of Geological Sciences, Brown University, Providence, RI 02912, USA

^e Department of Terrestrial Magnetism, Carnegie Institution of Washington, Washington, DC 20015, USA

^f School of Earth and Space Exploration, Arizona State University, AZ 85281, USA

^g Institute of Planetary Research, Deutsches Zentrum für Luft- und Raumfahrt, 12489 Berlin, Germany

ARTICLE INFO

Article history:

Received 5 December 2012

Revised 30 September 2013

Accepted 2 October 2013

Available online 15 October 2013

Keywords:

Cratering

Mercury, surface

Moon, surface

Impact processes

ABSTRACT

The impact cratering process is usually divided into the coupling, excavation, and modification stages, where each stage is controlled by a combination of different factors. Although recognized as the main factors governing impact processes on airless bodies, the relative importance of gravity, target and projectile properties, and impact velocity in each stage is not well understood. We focus on the excavation stage to place better constraints on its controlling factors by comparing the morphology and scale of crater-exterior structures for similar-sized fresh complex craters on the Moon and Mercury. We find that the ratios of continuous ejecta deposits, continuous secondaries facies, and the largest secondary craters on the continuous secondaries facies between same-sized mercurian and lunar craters are consistent with predictions from gravity-regime crater scaling laws. Our observations support that gravity is a major controlling factor on the excavation stage of the formation of complex impact craters on the Moon and Mercury. On the other hand, similar-sized craters with identical background terrains on Mercury have different spatial densities of secondaries on the continuous secondaries facies, suggesting that impactor velocity may also be important during the excavation stage as larger impactor velocity may also cause greater ejection velocities. Moreover, some craters on Mercury have more circular and less clustered secondaries on the continuous secondaries facies than other craters on Mercury or the Moon. This morphological difference appears not to have been caused by the larger surface gravity or the larger median impact velocity on Mercury. A possible interpretation is that at some places on Mercury, the target material might have unique properties causing larger ejection angles during the impact excavation stage. We conclude that gravity is the major controlling factor on the impact excavation stage of complex craters, while impact velocity and target properties also affect the excavation stage but to a lesser extent than gravity.

© 2013 Elsevier Inc. All rights reserved.

1. Introduction

Mercury's surface is populated by numerous impact craters, giving it a first-order appearance similar to the Moon (Murray et al., 1974). Fresh impact craters with pristine morphology (i.e., little eroded, distinct rims, and few superposed craters) and the distribution of their secondary craters (secondaries are formed by impacts of high velocity ejecta; Shoemaker, 1965) are windows into studying the factors that affect the impact cratering process,

such as the presence of an atmosphere, surface gravity, target and projectile properties, and impact velocity. Mercury and the Moon are airless bodies and thus are not affected by atmospheres, making these bodies ideal laboratories for comparative studies of impact processes (Gault et al., 1975; Schultz and Singer, 1980).

The impact process can be divided into the coupling, excavation, and modification stages (e.g., Gault et al., 1968; Melosh, 1989). The coupling stage begins at the instant when the impactor strikes the target surface and its kinetic energy is transmitted into the target material, inducing impact melting and vaporization. Outside the melting and vaporization zone, the expanding shock wave front severely damages and ejects the target material, marking the onset of the excavation stage. The shock fronts weaken

* Corresponding author at: Planetary Science Institute, Faculty of Earth Sciences, China University of Geosciences (Wuhan), #388 Lumo Road, Hongshan District, Wuhan, Hubei 430074, China.

E-mail address: xiaobeary@gmail.com (Z. Xiao).

rapidly with increasing distance from the melting and vaporization zone, accompanied by a rapid decrease of ejection velocities. The transient crater forms at the end of this stage. During the modification stage, the ejected material falls back to the surface and the transient crater collapses due to gravitationally unstable crater walls. As a result, the crater diameter grows while the depth decreases. The modification stage can take a longer time relative to the coupling and excavation stages (Melosh, 1989).

Early studies comparing the morphology and scale of craters on Mercury to the Moon focused primarily on crater interior structures, such as central peaks, crater depth, rim height, rim scallops, and wall terraces (e.g., Head, 1976; Oberbeck et al., 1977). Opinions have differed over the role of the above described factors on the size and morphology of impact structures on the Moon and Mercury. For example, Murray et al. (1974) suggested that for a similar-sized projectile, the larger median impact velocity on Mercury could overcome the greater surface gravity and form a larger crater as compared to the Moon. Gault et al. (1975) suggested that the primary cratering variable between the Moon and Mercury was gravitational acceleration. They considered different target-physical properties, impact velocities, possible thermal history, etc., to have potentially contributed to some degree, but thought the influence of those variables to be of second-order importance. Head (1976), Cintala et al. (1977) and Malin and Dzurisin (1978) argued that target properties might be one of the controlling factors, at least for the development of crater terraces and for the simple-to-complex crater transition diameter. Cintala et al. (1976) and Smith and Hartnell (1978) concluded that gravity, terrain type, and impact velocity were all important in affecting crater sizes on the terrestrial planets.

The controlling factors in each stage of a cratering event are not the same (e.g., Holsapple, 1993). Correspondingly, the morphology and size of different parts of an impact crater are controlled by different factors, i.e., the zonal approach described by Schultz (1976). For example, interior structures of fresh craters are initially formed by the impacts and subsequently modified by mass wasting or other processes (Melosh, 1989); crater interior structures record the effect of factors from the coupling to modification stage. In this sense, most of the earlier reported morphological differences between craters on the Moon and Mercury can only be used to study the relative importance of the different factors on the overall impact cratering process. However, a full understanding of impact processes requires studying the controlling factors in each of the three cratering stages and those for different crater terrains. For example, the controlling factors of the coupling stage are reflected in the amount of impact melt and vaporization (e.g., Cintala, 1992), and those of the modification stage are reflected in the size and morphology of interior structures (e.g., crater terraces; Pike, 1980).

Exterior structures of fresh impact craters (i.e., continuous ejecta deposits and secondaries field) form from the emplacement of excavated material and these structures are less affected by the latter modification stage compared with crater interior structures. They precisely record the impact excavation process and are ideal for studying the controlling factors in this stage. Previous studies compared crater exterior structures between lunar and mercurian craters and argued either that both gravity and impact velocity control the scale of these features (e.g., Pike, 1980; Schultz, 1988) or that gravity is the only controlling factor (Gault et al., 1975; Schultz and Singer, 1980). However, these studies used radial distances to represent the extents of crater exterior structures, which are usually not precise due to the asymmetric distribution of impact ejecta, and thus may bias the interpretation.

Early studies used Mariner 10 data to compare lunar and mercurian craters (e.g., Murray et al., 1975; Gault et al., 1975; Cintala et al., 1977). Mariner 10 data were of limited resolution and coverage (~45% of the surface at 1 km/pixel on average; Murray et al.,

1974) and included a large number of low incidence angle (>60°, measured from horizon) images (Strom, 1979), which restricted morphological analyses of impact craters. After three flybys, the MERCURY Surface, Space ENvironment, GEochemistry, and Ranging (MESSENGER; Solomon et al., 2001) spacecraft was successfully inserted into the orbit about Mercury in March 2011. The Mercury Dual Imaging System (MDIS; Hawkins et al., 2007) onboard MESSENGER has been carrying out systematic global imaging augmented by high-resolution targeted observations. At the conclusion of the one Earth-year primary mission, MESSENGER images covered over 99% of Mercury's surface. Images returned by MESSENGER have higher-resolution and better illumination conditions than the Mariner 10 imagery thus allowing an improved assessment of crater morphologies and associated landforms and, hence, providing a better basis to obtain insights into the impact process in the innermost parts of the Solar System.

In this study, we seek to investigate the importance of gravity, impact velocity, and target properties in the impact excavation process on the Moon and Mercury using the gravity-regime crater scaling laws and comparative studies. To achieve this goal, we measure the sizes of crater exterior structures for similar-sized craters on the Moon and Mercury using high-resolution images obtained by both the Lunar Reconnaissance Orbiter Camera (LROC; Robinson et al., 2010) and MDIS.

2. Objectives and methodology

2.1. Background and scope of the study

We focus on the excavation stage of impact cratering, schematically illustrated in Fig. 1, to better constrain its controlling factors. The impact process removes target material from the excavation cavity and deposits it beyond the crater rim. Earlier authors have used different methods to subdivide crater deposits into radial regions. For example, Gault et al. (1975) divided crater ejecta deposits into continuous ejecta and discontinuous facies. Schultz and Singer (1980) divided crater exteriors into continuous ejecta deposits, secondary chains, and discontinuous secondary fields. Here we adopt the method of Schultz and Singer (1980) and divide a fresh impact crater into four components radial to the crater center (Fig. 2): crater interior, continuous ejecta deposits, continuous secondaries facies, and discontinuous secondaries facies.

The continuous ejecta deposits exhibit no secondary clusters or chains. It starts at the rim crest of the primary crater, which consists of hummocky terrain, and grades outward into a radially ridged facies (Schultz and Singer, 1980). These two facies have no sharp boundaries and together they comprise the continuous ejecta deposits. The continuous secondaries facies is composed of secondary crater chains and/or clusters. Beyond a certain distance from the parent crater, secondaries are more isolated and they do not always occur in chains or clusters. This is the boundary between the continuous and discontinuous secondaries facies. The discontinuous secondaries facies is composed of relatively isolated secondaries that are caused by ejecta of relatively large ejection velocities, which are launched during the early excavation stage. Individual secondary craters in the discontinuous secondaries facies can be globally distributed (e.g., Melosh, 1989).

The layout and extent of ejecta deposits around impact craters are not only related to the excavation process, lateral ballistic sedimentation caused by the landing of ejecta (e.g., Oberbeck, 1975) and later modification processes (e.g., crater wall retreat; Gault et al., 1975) may also affect them. For fresh craters, the extents of their continuous ejecta deposits and continuous secondaries facies are mainly controlled by the trajectories of the emplaced materials. The trajectory properties on airless bodies include

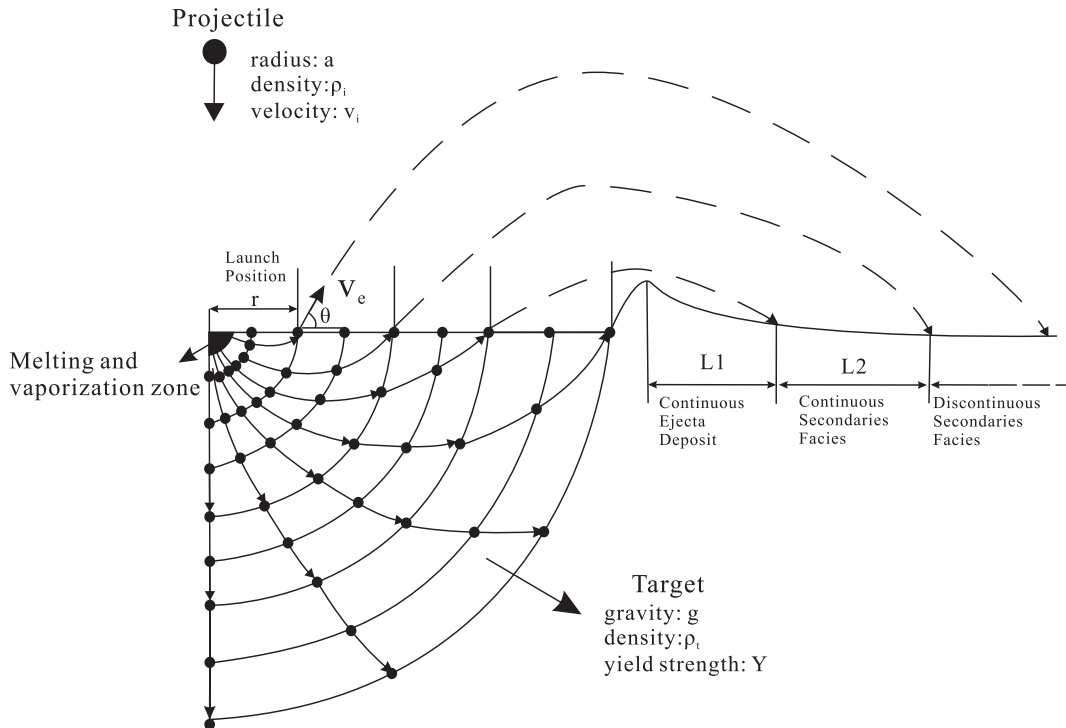


Fig. 1. Schematic illustration of the impact excavation processes showing the motion of particles in the excavation cavity. The parameter r is the launch position of ejecta to the impact point. θ is the ejection angle and v_e is the ejection velocity. L_1 is the average radial extent of the continuous ejecta deposit. L_2 is the average radial extent of the continuous secondaries facies. The seven arrowed solid lines represent hydrodynamic streamlines along which the excavated particles move in the excavation cavity. These streamlines are axially symmetric for a vertical impact, producing a “stream tube” in three dimensions (cf. Richardson et al., 2007). All particles in a given streamline will launch from the ground surface at the same distance r from the impact point with the same ejection velocity (Maxwell, 1977). Particles with the same radial distance to the impact point begin motion at the same speed when the shock fronts arrive. This figure is modified from Croft (1980) after the Maxwell-Z model (Maxwell, 1977).

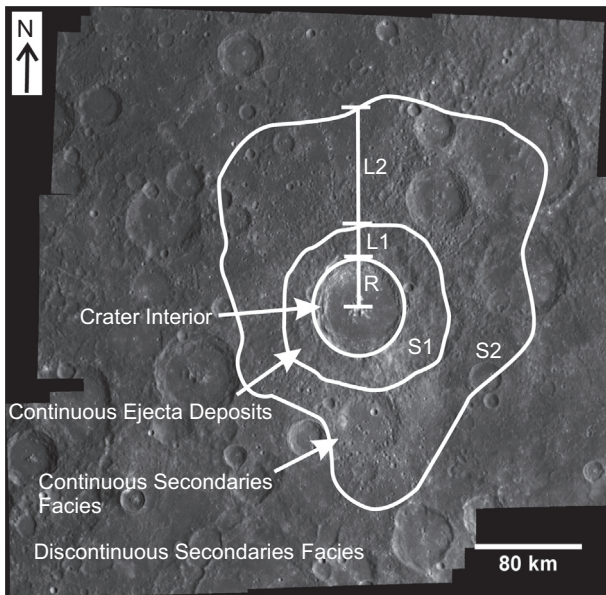


Fig. 2. An unnamed crater centered at 252°E, 0.7°S on Mercury has an asymmetric distribution of continuous ejecta deposits and continuous secondaries facies. The base mosaic is in sinusoidal projection. On planetary surfaces, few impact craters have a symmetric distribution for continuous ejecta or continuous secondaries facies. We used surface areas (S_1 and S_2) instead of radial extents to represent the scales for these respective deposits. R is the crater rim-to-rim radius, and L_1 and L_2 are the average radial extents of S_1 and S_2 , respectively.

launch positions (r), ejection velocity (v_e), and ejection angle (θ) as shown in Fig. 1. Impact velocity (v_i), target and projectile properties (Fig. 1), and surface gravity (g) affect these properties

(Holsapple, 1993). By comparing the extent of continuous ejecta deposits and continuous secondaries facies for similar-sized craters on the Moon and Mercury, we can investigate the relative importance of impact velocity, surface gravity, and target properties on the impact excavation process.

Previous studies used radial distances to represent the extents of continuous ejecta deposits and continuous secondaries facies. For example, Gault et al. (1975) measured distances from the outermost continuous ejecta deposits to crater rims to represent the extents of continuous ejecta deposits; Schultz and Singer (1980) applied the same method for continuous secondaries facies. However, radial distances do not accurately represent the size of these exterior structures because few projectiles vertically impact into horizontal target surfaces (cf., Hermalyne and Schultz, 2010). Although parent craters are circular in shape, the distribution of their impact deposits is rarely symmetric about the impact point (e.g., Gault and Wedekind, 1978; Schultz, 1992; Schultz et al., 2007). On planetary surfaces, the continuous ejecta deposits and continuous secondaries facies of an impact crater generally have different radial extents in different azimuth. Fig. 2 shows an example on Mercury. To precisely record the size of continuous ejecta deposits and continuous secondaries facies, we use surface areas instead of radial distances to represent the scale of the two crater exterior ejecta facies (S_1 and S_2 respectively, Fig. 2).

In addition, we try to interpret the observations by means of cratering mechanics using gravity-regime crater scaling laws. To accomplish this, the sampled craters are assumed to form from vertical impacts, so that the average radial extents of continuous ejecta deposits (L_1) and continuous secondaries facies (L_2) can be used in crater scaling calculations. L_1 and L_2 are calculated from S_1 and S_2 and the calculation method is introduced in Section 3.1.

During the impact cratering process, various-sized secondaries are produced on the continuous secondaries facies and their diameters range up to a maximum value of d_{max} . Sizes of secondaries on airless bodies are controlled by five parameters (Schultz and Singer, 1980): surface gravity, ejection angle, ejection velocity, ejecta size, and ejecta state (i.e., solid or dispersed; Schultz and Gault, 1985). These variables are related to the excavation process of the parent crater. Here we compare the diameters of the largest secondaries (d_{max}) on the continuous secondaries facies for similar-sized craters on Mercury and the Moon. The measurement is performed on the whole continuous secondaries facies for each crater. Additionally, the crater density of secondaries on continuous secondaries facies is determined by the number of secondaries and the surface area (i.e., $S2$). The surface area is affected by gravity and ejection velocities, which again provide insights into the excavation process. Therefore, we also compare the density of secondaries for several similar-sized craters on the Moon and Mercury.

2.2. Methodology

Fresh complex craters ($D > 20$ km) with sharp rims, pronounced secondaries, and no or few superposed small primary craters on the continuous ejecta deposits are selected for this study. They include the well-preserved morphological Class 1 craters according to Arthur et al. (1963) and Wood and Anderson (1978). Impact basins ($D < \sim 300$ km) with a fresh appearance are selected as well but they are not necessarily as young as the Class 1 craters. Different target materials on a planetary body may affect the morphology and scale of impact craters (e.g., Holsapple and Schmidt, 1979). Similar to previous studies that classified craters based on their background terrains (Trask and Guest, 1975; Cintala et al., 1977; Pike, 1980), on both the Moon and Mercury, craters on heavily cratered terrains and flooded-plains are treated separately.

Ten craters about 20–90 km in diameter on lunar mare, seventeen craters about 20–190 km in diameter on lunar highlands, twenty-one craters about 40–260 km in diameter on flooded-plains on Mercury, and thirty-two craters about 40–300 km in diameter on heavily cratered terrains on Mercury are included for the comparison. Table A1 in the appendix shows the detailed information (e.g., diameter, longitude and latitude) for these craters.

For the sampled craters on Mercury, MDIS mosaics are generated for each crater using the USGS's Integrated Software for Imagers and Spectrometers (<http://isis.astrogeology.usgs.gov/>). To preserve the accurate areal sizes of the continuous ejecta deposits and continuous secondaries facies, the mosaics are in sinusoidal projections and are centered on the crater centers. The image resolution is $\sim 80\text{--}250$ m/pixel.

We select fresh complex craters located in the equatorial to mid-latitude regions on the Moon (between 60°N and 60°S). The base mosaics for the lunar craters sampled are taken from the eight equatorial LROC WAC mosaics which have equirectangular projections and each encompasses 60 degrees of latitude by 90 degrees of longitude. A detailed description of the LROC mosaics is at http://wms.lroc.asu.edu/lroc/global_product/100_mpp_global_bw/about. Distortion in surface areas ($S1$ and $S2$) of the lunar craters is neglectable, because the measured crater rim-to-rim area is within an error of $\sim 15\%$ compared with the calculated crater rim-rim area based on the crater diameter value listed in JMars for the Moon (<http://jmars.asu.edu/>). This areal error corresponds to a less than $\sim 7\%$ error for the deduced crater diameter. Moreover, different illumination conditions may affect the interpretation of crater morphologies (e.g., Wilcox et al., 2005; Head et al., 2010; Ostrach et al., 2011). In this study, the LROC mosaics are taken at incidence angles of $69\text{--}82^{\circ}$ (refer to the surface normal). MDIS mosaics having the same range of incidence angles are selected.

Using the classification criteria of crater exterior structures introduced in Section 2.1, the publicly available image processing software ImageJ (<http://rsbweb.nih.gov/ij/>) is employed to outline different crater exterior structures, measure the $S1$, $S2$, and d_{max} , and perform crater counts of secondaries. All the raw data measured for this study are listed in the appendix Table A1.

3. Comparisons of spatial extent, morphological and geometrical properties of ejecta deposits on the Moon and Mercury

3.1. Areas of continuous ejecta deposits and continuous secondaries facies

To detect the possible effect of different target materials on the areas of continuous ejecta deposits ($S1$) and continuous secondaries facies ($S2$), on both the Moon and Mercury, we first compared the $S1$ and $S2$ for similar-sized craters on different types of terrain. In Fig. 3a, the areas of continuous ejecta deposits of similar-sized craters on lunar mare and lunar highlands are almost the same for craters larger than ~ 30 km in diameter. This is also true for the areas of continuous secondaries facies (Fig. 3a). However, in the diameter range of $\sim 20\text{--}200$ km, the fitted lines of both $S1$ vs D and $S2$ vs D are different between the sampled craters on lunar mare and lunar highlands (see parameters in Table 1). This difference may be caused by difficulties in determining the boundaries between the continuous ejecta deposits and continuous secondaries for craters smaller than ~ 30 km in diameter using the 100 m/pixel LROC global mosaic. Since only two of the ten craters on lunar mare are smaller than ~ 30 km in diameter (black circle in Fig. 3a; Table A1), the two examples will be excluded from the following comparisons of $S1$ and $S2$ between the craters on the Moon and Mercury. Moreover, due to the relatively young age of lunar mare compared with lunar highlands, less complex craters occur on mare surfaces thus restricting the number of the craters analyzed, especially at $D > \sim 100$ km. On Mercury, $S1$ of similar-sized craters on flooded-plains and heavily cratered terrains is almost the same as is for $S2$ (Fig. 3b). Therefore, on both the Moon and Mercury, different target properties, if they exist between heavily cratered terrains and flooded-plains on Mercury, have no significant effect on the $S1$ or $S2$ of similar-sized craters larger than ~ 30 km in diameter. However, the possible effect of the potentially different target materials between the Moon and Mercury still needs to be considered.

Craters on lunar highlands and mare were combined and compared with all the sampled craters on Mercury. Fig. 4a shows a comparison of $S1$ and $S2$ for the sampled craters on the Moon and Mercury. On average, lunar craters have both larger continuous ejecta deposits and continuous secondaries facies than similar-sized craters on Mercury. Correspondingly, lunar craters have larger surface areas from the outermost continuous secondaries facies to crater rim crests (i.e., $S1 + S2$; Fig. 4b). When D ranges from 30 to 200 km, the ratios of these values ($S1$, $S2$, and $S1 + S2$) between similar-sized mercurian and lunar craters are calculated using the best fit lines (the parameters are listed in Table 1):

$$\frac{S1_M}{S1_L} = 0.58\text{--}0.78, \quad \frac{S2_M}{S2_L} = 0.69\text{--}0.82, \quad \frac{(S1 + S2)_M}{(S1 + S2)_L} = 0.66\text{--}0.83. \quad (1)$$

$L1$ and $L2$ are the average radial extents of $S1$ and $S2$ respectively (Fig. 2). Based on the measured values of $S1$ and $S2$, $L1$ and $L2$ are calculated using:

$$S1 = \pi(R + L1)^2 - \pi R^2, \quad S2 = \pi(R + L1 + L2)^2 - \pi(R + L1)^2 \quad (2)$$

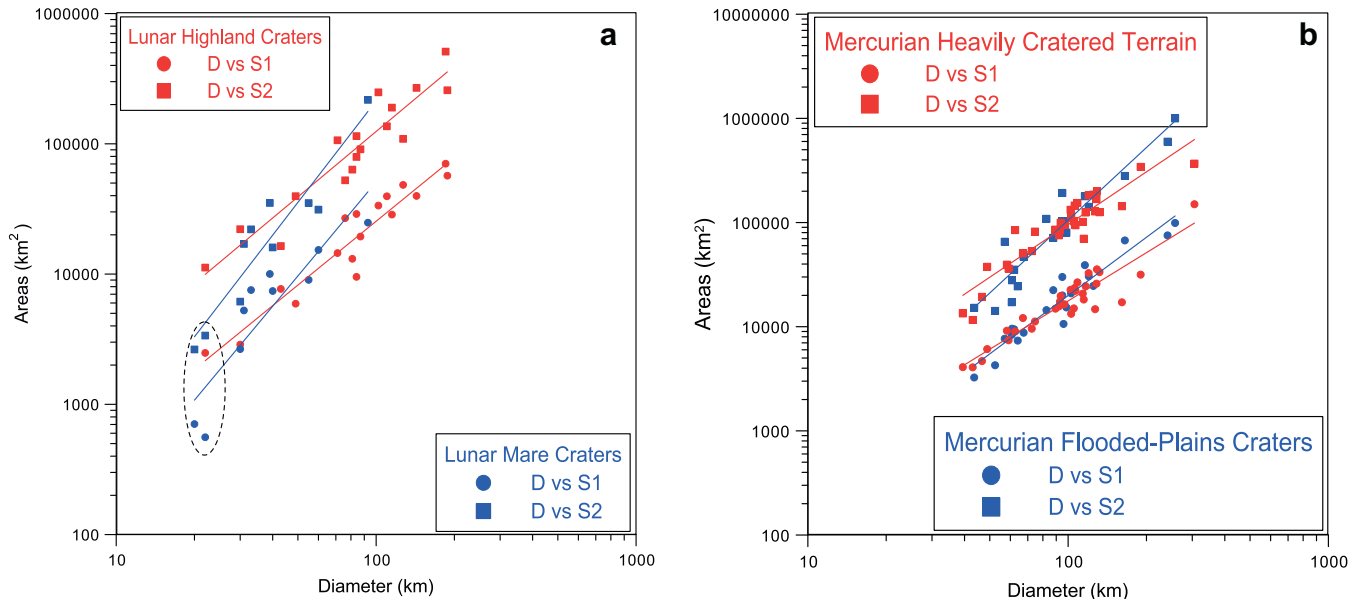


Fig. 3. Areas of continuous ejecta deposits (S1) and continuous secondaries facies (S2) shown as a function of crater rim-to-rim diameter in log-log space. (a) S1 and S2 of lunar craters; (b) S1 and S2 of mercurian craters. Craters on lunar maria and mercurian flooded-plains are blue, craters on lunar and mercurian heavily cratered terrains are red; dots are S1 and squares are S2. No significant difference is visible in the S1 or S2 for similar-sized craters on Mercury. It is also true for similar-sized craters larger than ~30 km on the Moon. The two craters on lunar mare smaller than 30 km in diameter fall below the fit lines (dashed circle in panel a). S2 is always larger than S1 for all the craters. The relationship between crater rim-rim diameter (D) and S1 and S2 (X) is fitted by: $X = a \times D^b$, where a and b are coefficients shown in Table 1. (For interpretation of the references to color in this figure legend, the reader is referred to the web version of this article.)

Table 1

Parameters for the best-fit relationships between crater rim-to-rim diameter and the calculated/measured crater aspects.

| Aspects | Coefficients of power-law fits ^a | | |
|---|---|------|-------|
| | a | b | R^2 |
| Lunar highlands S1 | 2.65 | 1.63 | 0.91 |
| Lunar highlands S2 | 4.05 | 1.67 | 0.88 |
| Lunar maria S1 | -0.2 | 2.34 | 0.81 |
| Lunar maria S2 | 0.34 | 2.59 | 0.88 |
| Mercurian heavily cratered terrains S1 | 2.68 | 1.54 | 0.87 |
| Mercurian heavily cratered terrains S2 | 3.73 | 1.68 | 0.86 |
| Mercurian flooded-plains S1 | 1.33 | 1.86 | 0.91 |
| Mercurian flooded-plains S2 | 0.87 | 2.32 | 0.90 |
| Lunar S1 | 3.19 | 1.52 | 0.88 |
| Lunar S2 | 3.20 | 1.86 | 0.87 |
| Mercurian S1 | 2.12 | 1.67 | 0.88 |
| Mercurian S2 | 2.52 | 1.95 | 0.86 |
| Lunar S1 + S2 | 3.72 | 1.79 | 0.90 |
| Mercurian S1 + S2 | 2.90 | 1.91 | 0.88 |
| Lunar L1 | 1.43 | 0.56 | 0.64 |
| Lunar L2 | 0.28 | 0.98 | 0.77 |
| Lunar L1 + L2 | 1.34 | 0.83 | 0.84 |
| Mercurian L1 | 0.30 | 0.74 | 0.71 |
| Mercurian L2 | -0.41 | 1.07 | 0.69 |
| Mercurian L1 + L2 | 0.44 | 0.97 | 0.79 |
| Lunar highlands d_{max} | -6.27 | 1.72 | 0.84 |
| Lunar maria d_{max} | -5.41 | 1.51 | 0.91 |
| Mercurian heavily cratered terrains d_{max} | -3.28 | 1.11 | 0.92 |
| Mercurian flooded-plains d_{max} | -3.57 | 1.17 | 0.82 |
| Lunar d_{max} | -5.81 | 1.60 | 0.92 |
| Mercurian d_{max} | -3.39 | 1.13 | 0.86 |

^a Power laws are of the form $X = e^a \times D^b$, where X represents sizes of crater aspects measured (i.e., S1 and S2) and calculated ($L1$ and $L2$) in this study a and b are coefficients, D is the crater rim-to-rim diameter. R -squared (R^2) is the coefficient of determination.

where $R = D/2$ is the crater radius. Fig. 4c shows the comparison of $L1$ and $L2$ for the sampled craters. We find that on average, craters on Mercury have smaller radial extents of both continuous ejecta

deposits and continuous secondaries facies than similar-sized lunar craters. The individual data points are rather scattered, as the coefficients of determination (R^2) are relatively small (Table 1). It indicates that on both Mercury and the Moon, similar-sized craters have different average radial extents of continuous ejecta deposits and continuous secondaries facies. When D is between 30 and 200 km, the ratios of $L1$ and $L2$ for similar-sized craters on Mercury and the Moon is calculated using the best fit lines (Table 1).

$$\frac{L1_M}{L1_L} = 0.60 - 0.84, \frac{L2_M}{L2_L} = 0.68 - 0.81 \quad (3)$$

The results shown in Eqs. (1) and (3) confirm previous findings that craters on Mercury have smaller continuous ejecta deposits and continuous secondaries facies which were ascribed to the larger surface gravity on Mercury (e.g., Murray et al., 1974, 1975; Guest and O'Donnell, 1977). Notably, Gault et al. (1975) measured the $L1$ for similar-sized craters on Mercury and the Moon and found $\frac{L1_M}{L1_L} = 0.65$. This value is within the range of our observation in Eq. (3), but the latter has a larger value range indicating that some craters on Mercury can form larger than expected continuous ejecta deposits and continuous secondaries facies.

The average radial extents from the outermost continuous secondaries facies to crater rims ($L1 + L2$) are calculated and compared in Fig. 4d. These values will be used later when relating our observations to crater scaling relationships (Section 4). Eq. (4) lists the ratio of $L1 + L2$ between similar-sized craters on Mercury and the Moon.

$$\frac{(L1 + L2)_M}{(L1 + L2)_L} = 0.61 - 0.76 \quad (4)$$

In general, our observed extents of continuous ejecta deposits and continuous secondaries facies are consistent with previous findings (e.g., Gault et al., 1975) and show the importance of gravity during the impact excavation process. However, the two ejecta facies of some mercurian craters are larger than expected

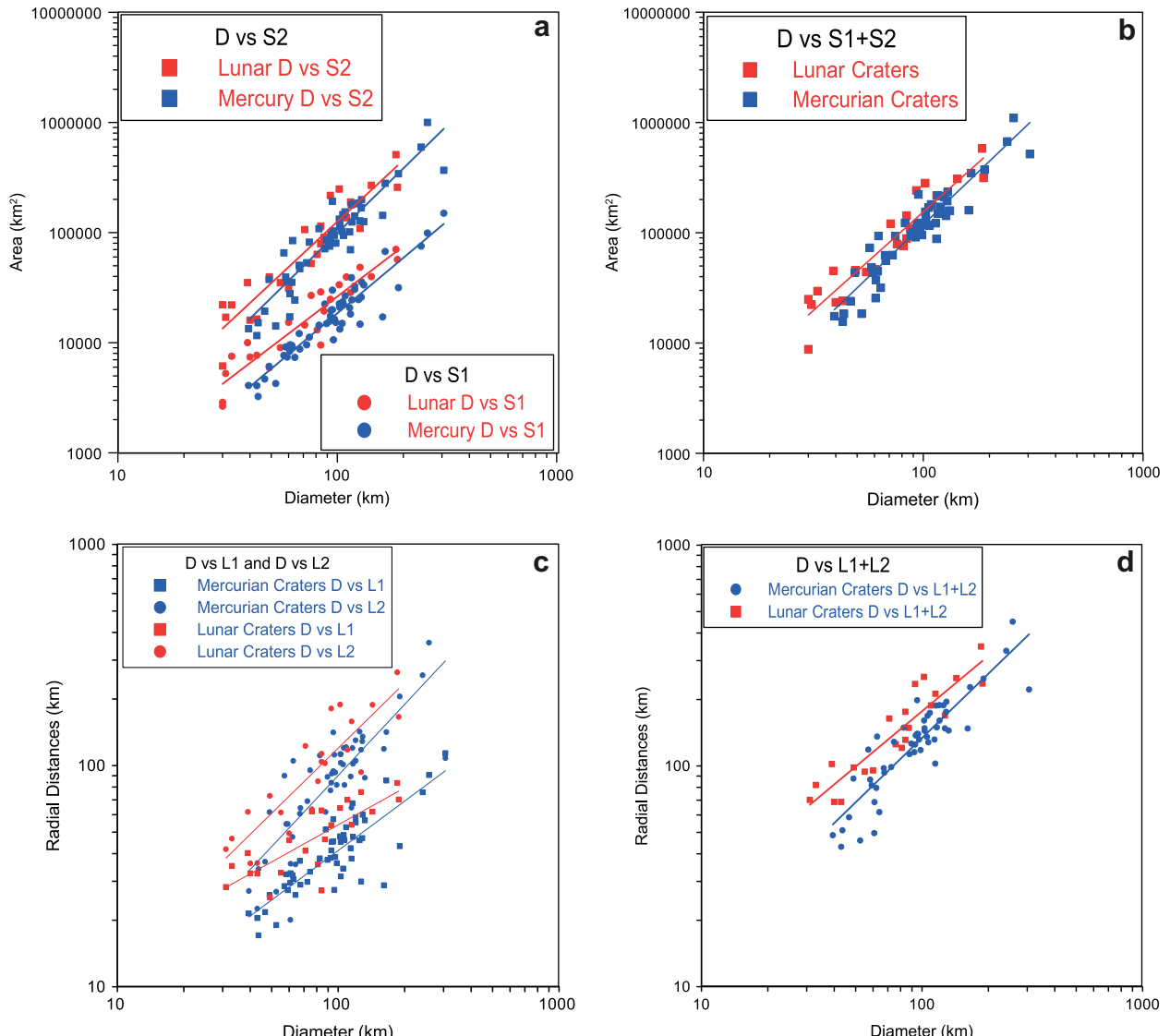


Fig. 4. (a) Comparison of $S1$ (dots) and $S2$ (squares) between mercurian (blue) and lunar (red) craters. Lunar craters have both larger $S1$ and $S2$ than that of similar-sized mercurian craters. (b) Comparison of surface areas from the outermost continuous secondaries facies to crater rim crests ($S1 + S2$) between lunar (red) and mercurian craters (blue). (c) Comparison of the average radial extents of the continuous ejecta deposits ($L1$, squares) and that of the continuous secondaries facies ($L2$, dots) between lunar (red) and mercurian (blue) craters. The points are rather scattered (Table 1). On average, lunar craters have larger $L1$ and $L2$ than similar-sized mercurian craters. (d) Comparison of the average radial extents from the outermost continuous secondaries facies to crater centers ($L1 + L2$) between lunar (red) and mercurian craters (blue). The relationships between crater rim diameter D and $S1$, $S2$, $L1$, $L2$, and $L1 + L2$ (X) are fitted by: $X = a \times D^b$, in which a and b are coefficients as shown in Table 1. All diagrams are in log-log space. (For interpretation of the references to color in this figure legend, the reader is referred to the web version of this article.)

indicating that some other processes also affect their sizes (see Section 4 for a detailed discussion).

3.2. Morphology and spatial distribution of secondaries

Typical lunar secondaries have extensive herringbone structures, downrange ejecta fans, ridge-like rims, and floor mounds (e.g., Oberbeck and Morrison, 1974). These characteristics are most common on the continuous secondaries facies because secondaries in these regions mostly occur in chains and/or clusters (e.g., Schultz and Gault, 1985). Some secondary chains even resemble troughs due to their close spacing. Schultz and Singer (1980) compared the circularity of secondaries for the Alencar crater on Mercury and the Copernicus crater on the Moon. They measured the long and short axis for eleven Copernicus secondaries and five Alencar secondaries and took the long-short axis ratio as the

circularity. Their results indicated that some of Alencar's secondaries had a slightly larger circularity than Aristarchus's secondaries (Schultz and Singer, 1980). However, the statistic was based on limited samples and large uncertainties exist in measuring the axis of highly irregularly-shaped lunar secondaries.

On Mercury, we find that although secondaries appear to be closer to the rim crest of their parent craters, secondaries on the continuous secondaries facies of some craters are more isolated from each other and more circular in shape. The present work does not attempt to quantitatively compare the long-/short-axis ratio as the ellipticity of lunar or mercurian secondaries because of their highly-irregular shapes. Here we offer a qualitative comparison. Fig. 5 shows two pairs of morphological comparisons of secondaries between craters on the Moon and Mercury that have same transient diameters (see Eq. (10) for the size relation between transient crater and final crater). The Copernicus crater ($D = 93$ km; 10°N ,

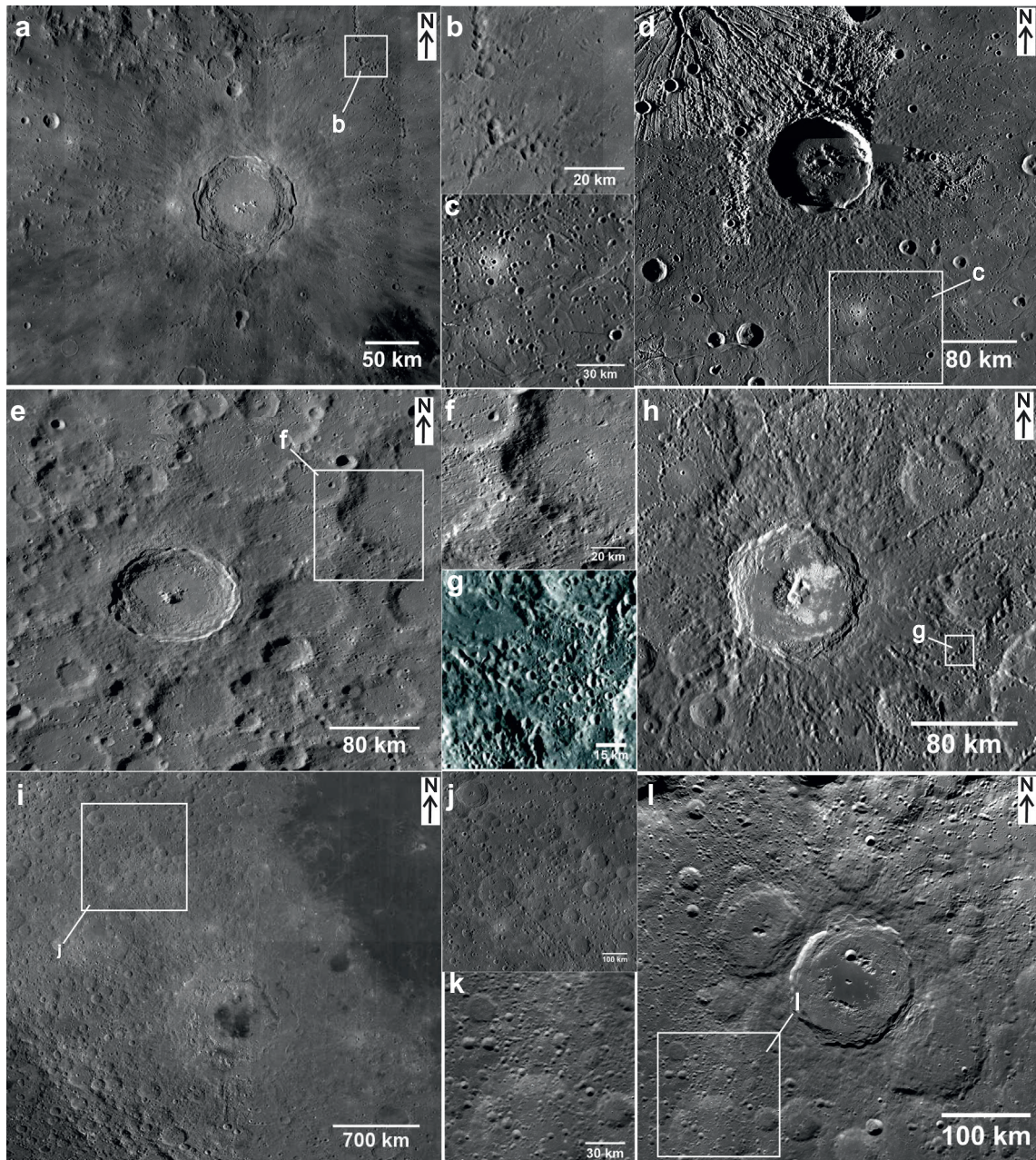


Fig. 5. Morphological comparison of secondaries on the Moon and Mercury. (a, b) The Copernicus crater on lunar mare has highly irregular-shaped secondaries. The base mosaic is from the LROC WAC_GLOBAL_E300N3150. (c, d) The Atget crater on the Caloris interior plains on Mercury has circular and isolated secondaries. The base image is from the global monochrome mosaics of Mercury that is in equirectangular projection (250 m/pixel). (e, f) Secondaries of the Tycho crater that in the lunar highlands have typical herringbone morphologies. The base mosaic is from LROC WAC_GLOBAL_E300S3150. (g, h) Tyagaraja on heavily cratered terrains on Mercury has some circular secondaries. (i, j) The Orientale basin on the Moon has circular secondaries similar to those on Mercury. The base image is from LROC WAC_GLOBAL_E300S2250_100M, WAC_GLOBAL_E300S3150_100M, WAC_GLOBAL_E300N2250_100M, and WAC_GLOBAL_E300N3150_100M. (k, l) The Antoniadi crater in the Southern Pole Aitken Basin has circular secondaries. Figures in (b, c, f, g, j and k) show parts of the continuous secondaries facies of the above six craters respectively. The LROC mosaics are in equirectangular projection and are 100 m/pixel in resolution.

20°W; Fig. 5a) is located on lunar mare and the Atget crater ($D = 103$ km; 26°N, 166°E; Fig. 5d) is located on the Caloris interior plains on Mercury (Murchie et al., 2008; Strom et al., 2008). Fig. 5b and c are parts of the continuous secondaries facies of Copernicus and Atget, respectively. The secondaries of Copernicus are highly irregular in shape, and most of them occur in clusters and/or chains (Fig. 5b). In contrast, most of Atget's secondaries are more circular and isolated from each other, although some occur in chains as well (Fig. 5c). The difference in the circularity of secondaries is also visible for similar-sized craters on heavily cratered surfaces

between the Moon and Mercury. For example, Fig. 5e is the lunar crater Tycho ($D = 86$ km; 43°S, 11°W) and Fig. 5h is the Tyagaraja crater on Mercury ($D = 97$ km; 4°N, 149°W). Secondaries of Tycho on the continuous secondaries facies occur in chains and clusters and have typical herringbone morphologies (Fig. 5f). Tyagaraja also has pronounced secondary chains. However, many of its secondaries have a circular shape and are more isolated from each other (Fig. 5h).

Craters having circular secondaries occur on both lava-flooded plains and heavily cratered terrains on Mercury. They are

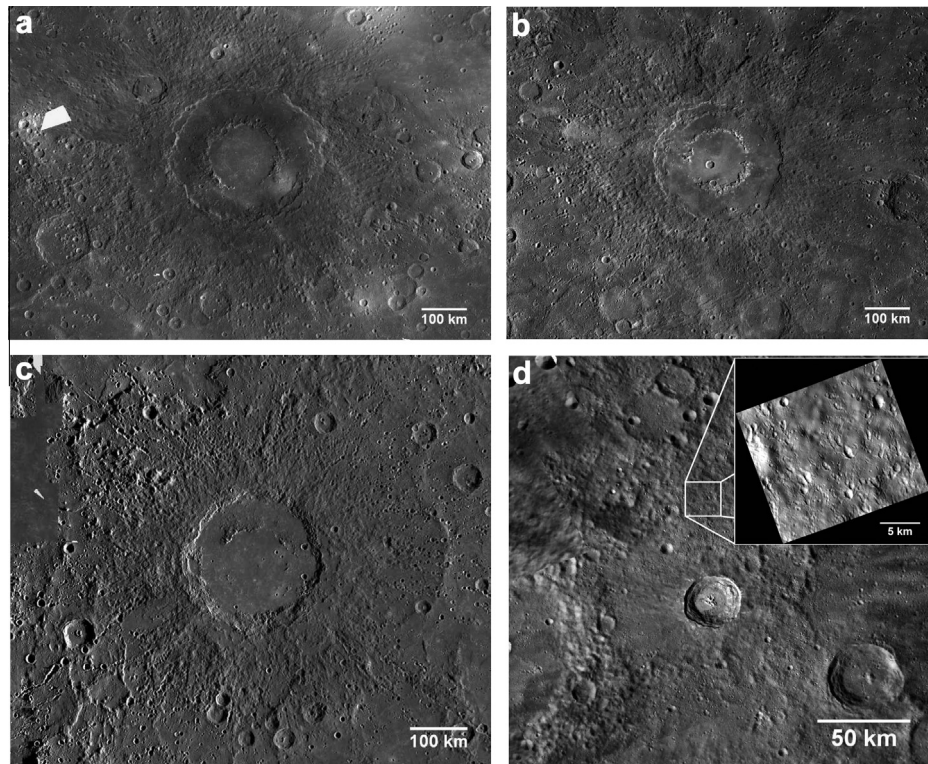


Fig. 6. Some fresh impact basins on Mercury have circular secondary craters on their continuous secondaries facies, such as Rachmaninoff (a), Raditladi (b), and Mozart (c). The secondaries are spatially isolated from each other. Some other craters on Mercury have highly irregularly-shaped secondaries on the continuous secondaries facies, which are similar with typical secondaries on the Moon. (d) A fresh crater ($D = 30$ km diameter; 33°N , 96°E) on Mercury have irregularly-shaped secondaries on the continuous secondaries facies. The inset image (EN0236702523M, sinusoidal projection) shows the detailed morphology for the secondaries. The base mosaics in (a–d) are from the global MDIS map of Mercury that are in equirectangular projection (250 m/pixel).

commonly associated with fresh impact basins, such as Rachmaninoff ($D = 306$ km; 28°N , 58°E ; Fig. 6a), Raditladi ($D = 258$ km; 27°N , 119°E ; Fig. 6b), and Mozart ($D = 241$ km; 8°N , 170°E ; Fig. 6c). However, not all craters on Mercury have such circular and isolated secondaries. For example, Fig. 6d shows a crater on Mercury having irregularly-shaped secondaries that highly resemble those on the Moon. On the contrary, very few lunar craters or basins have such circular secondaries, examples include the Orientale basin and the Antoniadi crater located inside the South Pole Aitken basin (Fig. 5i–l), but no lunar craters sampled for this study have similar circular and isolated secondaries on the continuous secondaries facies.

3.3. Diameters of the largest secondaries on continuous secondaries facies

We measure the diameter of the largest secondaries (d_{\max}) on the continuous secondaries facies for each of our sampled craters. For both the Moon and Mercury, craters on heavily cratered terrains and volcanic smooth plains are separated and their d_{\max} are compared. Fig. 7 shows that the d_{\max} of similar-sized craters on lunar highlands and lunar mare is almost the same (Fig. 7a). A similar trend is observed for the craters on Mercury (Fig. 7b). This indicates that different target materials on each planetary body do not have an obvious effect on the size of the largest secondaries. However, the effect of different target materials between the Moon and Mercury on d_{\max} needs to be considered. Notably, the lunar data points are relatively scattered at $D < \sim 40$ km for both the mare and highland craters (Table 1). This may be caused by relatively large errors in measuring the d_{\max} for craters smaller than ~ 40 km diameter using the 100 m/pixel LROC mosaics. These

craters (4 of the 27 lunar craters sampled) will not be used in the comparison of d_{\max} with the sampled craters on Mercury.

The d_{\max} of all the sampled craters on the Moon and Mercury are compared. Fig. 7c shows that on average, the d_{\max} of craters on Mercury is larger than that of the similar-sized lunar craters at $D < \sim 170$ km. At larger diameters, the d_{\max} is almost the same for similar-sized craters on the two bodies. The paucity of large and fresh impact basins on the Moon did not allow for a comparison of d_{\max} at $D > 170$ km (Table A1). When $D = 40$ – 170 km, the ratio of d_{\max} between similar-sized mercurian and lunar craters is:

$$\frac{d_{\max}^M}{d_{\max}^L} = 1.0\text{--}2.0 \quad (5)$$

Schultz and Singer (1980) compared the size-range distribution of secondaries on the continuous secondaries facies for the lunar craters Copernicus ($D = 93$ km) and Aristarchus ($D = 40$ km) with the Alencar crater ($D = 116$ km) on Mercury. Their measurements were performed within a 30° sector of the continuous secondaries facies for each crater (the whole continuous secondaries facies is 360°), and they found that within a radial distance of four times crater radius ($4R$), the d_{\max} of Copernicus was slightly larger than that of the similar-sized crater Alencar, and that the d_{\max} of Aristarchus was the smallest. But beyond $4R$, d_{\max} for Alencar was the largest for that particular dataset. Our measurements were based on the entire continuous secondaries facies for each crater and the results suggest that at $D < \sim 170$ km, craters on Mercury have larger secondaries on average in comparison with similar-sized lunar craters (Fig. 7c). Specifically, in our measurements, the d_{\max} of

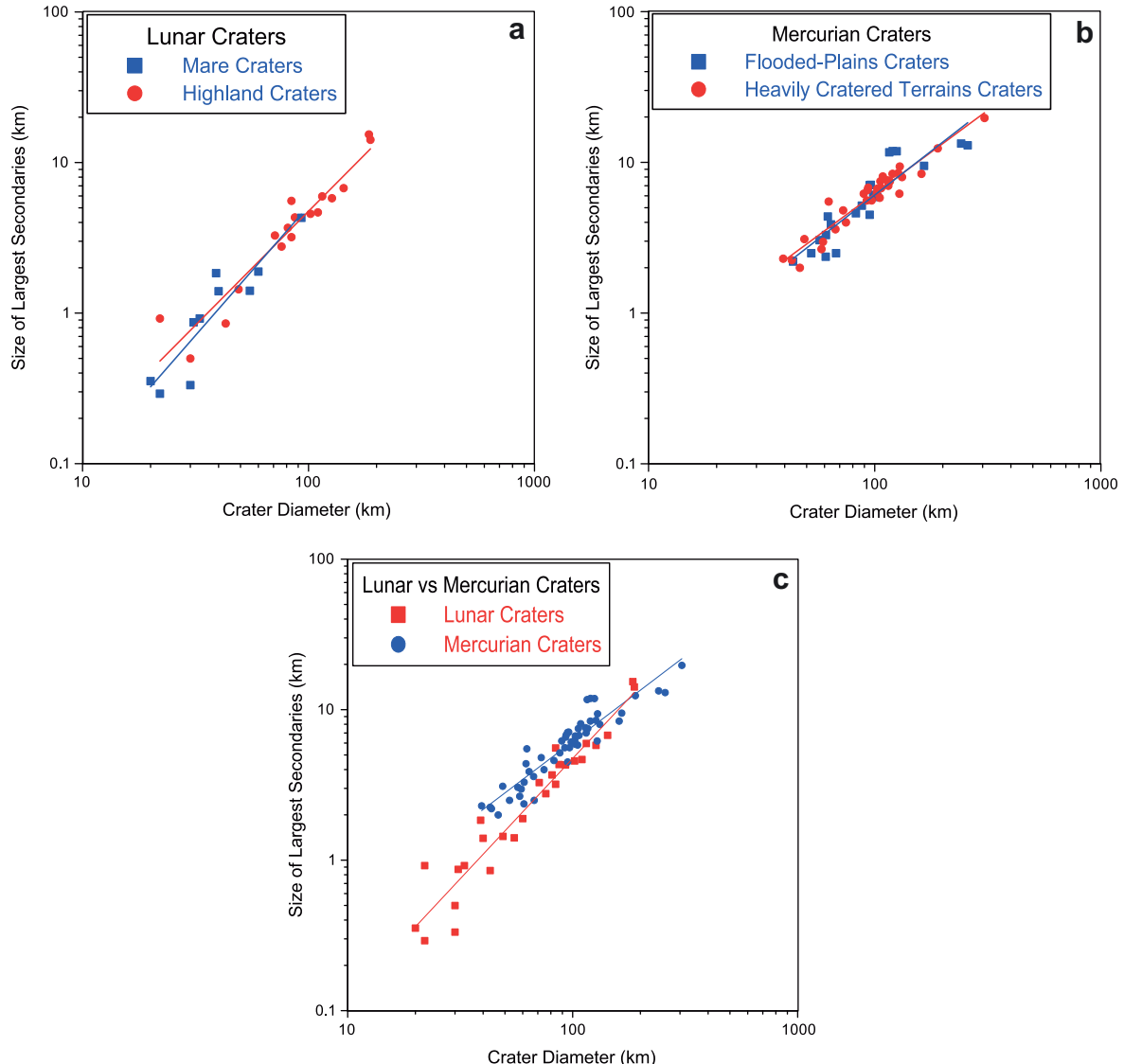


Fig. 7. (a) d_{max} of craters on lunar maria (blue squares) and lunar highlands (red dots); (b) d_{max} of craters on mercurian volcanic plains (blue squares) and heavily cratered terrains (red dots). On both the Moon and Mercury, no significant differences are visible in the d_{max} of similar-sized craters with different background terrains. (c) Comparison of d_{max} between lunar (red squares) and mercurian (blue dots) craters. Craters on Mercury have larger d_{max} than similar-sized lunar craters at $D < \sim 170$ km. The relationship between D and d_{max} is fit by: $d_{max} = a \times D^b$, in which a and b are coefficients as shown in Table 1. Diagrams are in log-log space. (For interpretation of the references to color in this figure legend, the reader is referred to the web version of this article.)

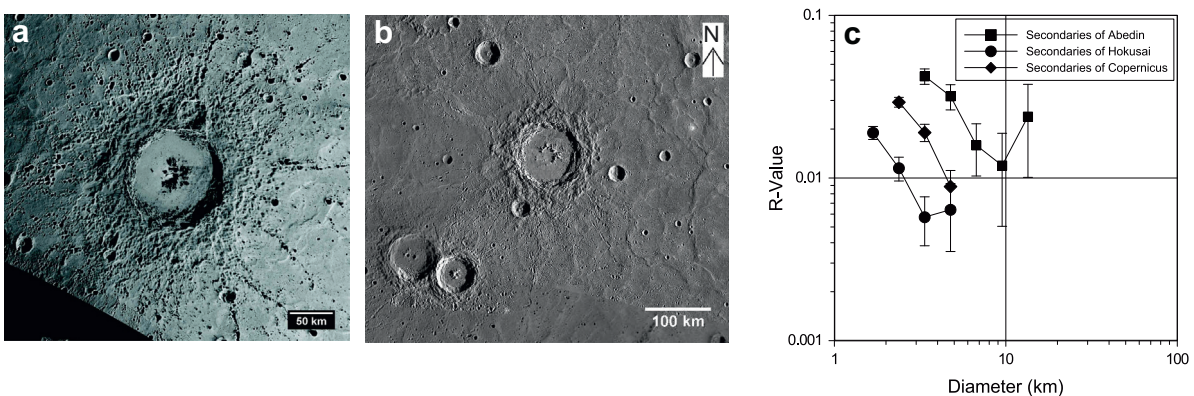


Fig. 8. (a) Abedin in the northern volcanic plains on Mercury. The base mosaic is in sinusoidal projection. (b) Hokusai crater in the northern volcanic plains of Mercury. The base mosaic is in sinusoidal projection. (c) R plot of the size-frequency distributions of secondaries on the continuous secondaries facies of Copernicus (diamonds), Abedin (squares) and Hokusai (dots). See a detailed discussion for the comparison in Section 3.4.

Table 2

Summary of the observed differences for the exterior structures of similar-sized craters on the Moon and Mercury.

| Compared items | | Moon | Mercury |
|-------------------|---|---|---|
| Primary craters | Areal extents of continuous ejecta deposits ($S1_L$ ^a) Areal extents of continuous secondaries facies ($S2_L$ ^a) | $S1_L > S1_M$ $S2_L > S2_M$ | |
| Secondary craters | Circular morphology Distribution Spatial density d_{max} | Rare Highly clustered Abedin > Copernicus > Hokusai $d_{max}^L < d_{max}^M$ ^c | Exist ^b Less clustered ^b |

^a $S1$ and $S2$ are shown in Fig. 2 and the relations are expressed in Eq. (1).^b Not all mercurian craters have circular and isolated secondaries.^c This relation is for $D < \sim 170$ km (Eq. (5)).

Copernicus is 4.3 km, that of Aristarchus is 1.4 km, and that of Alencar is 7.5 km (Table A1).

3.4. Density of secondaries on continuous secondaries facies

We compared the spatial density of secondaries on continuous secondaries facies for several similar-sized craters on the Moon and Mercury. Copernicus on the Moon ($D = 93$ km; Fig. 5a), Abedin ($D = 116$ km; Fig. 8a) and Hokusai ($D = 95$ km; Fig. 8b) on Mercury were chosen for the comparison. The density and crater size-frequency distribution of the secondaries are presented in R plot¹ (Arvidson et al., 1979). Fig. 8c shows the results. We find that all the crater size-frequency distribution curves are steep with a differential slope of about -4 . This slope is typical for secondary crater populations on inner Solar System bodies (e.g., Shoemaker, 1965; Xiao and Strom, 2012). Moreover, the steep segments of the curves are sub-parallel to each other (Fig. 8c), with Abedin having the highest spatial density of secondaries, followed by Copernicus and then Hokusai.

Qualitatively, most craters on Mercury appear to have a higher density of secondaries on the continuous secondaries facies than similar-sized lunar craters because the secondaries appear to be more proximal to rim crests of their parent craters on Mercury. Previous studies also noticed this tendency (Murray et al., 1974; Gault et al., 1975; Guest and O'Donnell, 1977; Scott, 1977). Melosh (1989) noted that "Mercury's two times greater gravity restricts the secondaries crater range to roughly half the lunar value and raises the crater density to nearly four times that of the Moon." These findings are verified by our observation that Abedin has a density of secondaries approximately two to four times larger than Copernicus (Fig. 8c).

However, the spatial density of Hokusai's secondaries is lower than that of the secondaries of Copernicus. This cannot be explained by the larger surface gravity on Mercury and it is contrary to previous findings (Melosh, 1989). Moreover, Abedin and Hokusai have a similar diameter and both of the craters are located on the northern volcanic plains (Head et al., 2011). Abedin has a crater density of secondaries about three to eight times higher than that of Hokusai. The unexpected low density of secondaries of Hokusai compared to that of similar-sized craters on the Moon and Mercury (i.e., Copernicus and Abedin) suggests that some factors might have caused either a larger continuous secondaries facies of Hoku-

sai and/or a smaller population of secondaries on that facies (see Section 4 for a detailed discussion).

4. Discussion

Some of the findings in this paper (Table 2) support previous conclusions emphasizing the importance of the larger surface gravity on Mercury to the excavation stage. For example, craters on Mercury have smaller continuous ejecta deposits and continuous secondaries facies than similar-sized lunar craters; Abedin has a larger spatial density of secondaries on its continuous secondaries facies than the similar-sized Copernicus crater. However, some of our results cannot be solely explained by the larger surface gravity on Mercury.

In this section, we attempt to interpret our observations in Table 2 with respect to gravity-regime crater scaling laws. We confirm previous findings that gravity is the major controlling factor on the impact excavation stage of lunar and mercurian complex craters. Target properties and impact velocities are also important in the excavation stage, but their importance may be relatively small.

4.1. Gravity-regime scaling laws of impact cratering

Numerous power-law scaling relations of impact cratering have been mathematically derived from experimental impacts and point-source solutions. We used the Buckingham π theorem (e.g., Buckingham, 1914) for the impact excavation process of the primary craters studied here, which is related to seven parameters (Fig. 1; Housen et al., 1983): radius of projectile (a), impact velocity of projectile (v_i), target yield strength (Y), surface gravity (g), ejecta launch positions (r), and mass densities of projectile (ρ_i) and target (ρ_t). Assuming impactors on both the Moon and Mercury have the same physical properties, here we only consider the possible effect from potentially different target properties on these two bodies. Table A2 in the appendix lists several parameters of target properties (Holsapple, 1993). Since our studied craters are complex craters ($D > 20$ km) that are larger than the simple-to-complex crater transition diameters on both the Moon and Mercury, surface gravity instead of target strength (Y) controls the impact processes (cf. Holsapple, 1993). Generally, Y is not considered in the gravity-regime crater scaling laws (e.g., Housen et al., 1983).

Transient craters form at the end of the excavation stage when the excavation cavities reach the largest in both diameter and volume. Using the gravity-regime crater scaling laws, the volume of a transient crater (V) is defined (Holsapple and Schmidt, 1987; Holsapple, 1993) in the following equation:

$$V = K_1 \left(\frac{m_i}{\rho_t} \right) \left(\frac{ga}{v_i^2} \right)^{\frac{3\mu}{2+\mu}} \left(\frac{\rho_t}{\rho_i} \right)^{\frac{\mu}{2+\mu}}. \quad (6)$$

¹ On an R plot, crater size-frequency distribution is normalized to a power law differential size-frequency distribution function, $dN(D) \sim D^p dD$ where D is diameter. $p = -3$ because most crater size distributions are observed to be within ± 1 of a $p = -3$ power law distribution. A $p = -3$ distribution plots as a horizontal straight line; a $p = -2$ distribution slopes down to the left at an angle of 45° , and a $p = -4$ distribution slopes down to the right at 45° . The vertical position of the curve (R value) is a measure of crater density or relative age on the same planet; the higher the vertical position, the higher the crater density and the older the surface (Strom et al., 2005).

K_1 is a constant relating to the target material properties (Table A2). m_i is the mass of the projectile, which is expressed in the following equation:

$$m_i = \frac{4\pi}{3} \rho_i a^3. \quad (7)$$

Ideally, V can also be expressed by a function of the diameters of transient craters (D_t):

$$V = \frac{1}{24} \pi D_t^3. \quad (8)$$

The transient crater will be modified by collapse, e.g., slumping by dynamic collapse or dynamic floor rebound (e.g., Gault et al., 1975). Empirically, the relationship between the diameters of transient craters and those of the final craters (D) is defined as (Croft, 1985):

$$D = 1.3D_t; \text{ if } D_t \leq \frac{D_0}{1.3}. \quad (9)$$

$$D = 1.4 \frac{D_t^{1.18}}{D_0^{0.18}}; \text{ if } D_t \geq \frac{D_0}{1.3}. \quad (10)$$

D_0 is the transition diameter from simple to complex craters. On Mercury, $D_0 = 10.3$ km (Pike, 1988); for lunar craters, $D_0 = 15–20$ km (Pike, 1977) and we take $D_0 = 17.5$ km.

Ideally, during the impact excavation stage, ejecta are thrown out of the excavation cavity following the Maxwell Z-model (Fig. 1; Maxwell, 1977). Ejection velocity v_e is related to the launch position r that is measured from the impact point (Fig. 1; cf. Richardson et al., 2007) as:

$$v_e(r) = \frac{\sqrt{2}}{C_T} \frac{\mu}{\mu+1} \sqrt{gR_t} \left(\frac{r}{R_t} \right)^{-\frac{1}{\mu}}. \quad (11)$$

C_T is a constant value from 0.75 to 0.95, and here we employ the median value 0.85. R_t is the radius of the transient crater that equals $D_t/2$. Theoretically, the value of launch position r is smaller than R_t and larger than zero (Fig. 1).

Once fragments of ejecta are launched, most of them follow ballistic trajectories before falling back to the surface. The relationship between the horizontal travel distance of ejecta (R_e) and the ejection angle θ is given by (Melosh, 1989):

$$R_e = 2R_p \tan^{-1} \left(\frac{(v_e^2/R_p g) \sin \theta \cos \theta}{1 - (v_e^2/R_p g) \cos^2 \theta} \right), \quad (12)$$

where R_p is the radius of the target body, the Moon ($R_p = 1737$ km) and Mercury ($R_p = 2440$ km) in our case. If $R_e \ll R_p$, Eq. (12) can be abbreviated as follows:

$$R_e = \frac{v_e^2}{g} \sin 2\theta. \quad (13)$$

In this study, Eq. (13) can be used to calculate the radial extents of the continuous ejecta deposits because $L1$ are at least an order of magnitude smaller than the radius (R_p) of the Moon and Mercury (Fig. 4c). For the same reason, we need Eq. (12) to calculate the radial extents of the continuous secondaries facies because some of them are as large as 400 km (Fig. 4d).

Although ejection angles during a cratering process may vary from $\sim 27^\circ$ to 63° (Maxwell and Seifert, 1974; Anderson et al., 2004; Richardson et al., 2007), experimental impact simulations show that ejection angles are mostly between 40° and 45° (e.g., Gault et al., 1968; Hermalyn and Schultz, 2010), so $\sin 2\theta$ is close to 1. Therefore, Eq. (13) is usually abbreviated as:

$$R_e = \frac{v_e^2}{g}. \quad (14)$$

Eqs. (6)–(14) are derived from gravity-regime crater scaling laws relating to impact mechanics (Fig. 1). We will apply this set of equations in Sections 4.2 and 4.3 to our measurements and results (Table 2) to evaluate whether or not gravity is the only controlling factor in the impact excavation stage, and to analyze the relative contribution of impact velocity and target properties.

4.2. The effect of surface gravity on impact excavation processes

For similar-sized craters ($D > 20$ km) on the Moon and Mercury, the diameter ratio of their transient craters (D_t) is calculated from Eq. (10):

$$\frac{D_{t_M}}{D_{t_L}} = 0.92. \quad (15)$$

Craters on Mercury have smaller transient diameters than same-sized lunar craters. Meanwhile, Ostrach et al. (2012) found that when $D > \sim 40$ km, craters on Mercury have a larger region covered by impact melt than similar-sized lunar craters. If this observation is due to a larger amount of impact melt caused by the larger median impact velocity on Mercury, their melting and vaporization zone is larger compared with that of similar-sized lunar craters (Fig. 1). With this assumption, impact ejecta are launched from a smaller area in the excavation cavity of mercurian craters than those of similar-sized lunar craters.

From Eqs. (6)–(11), we derive the relationship of ejection velocity (v_e) and final crater diameter (D) with the launch position (r) as a variable:

$$v_e(D) = \frac{\sqrt{2}}{C_{Tg}} \frac{\mu}{\mu+1} \sqrt{g} r^{-\frac{1}{\mu}} \left(\frac{D * D_0^{0.18}}{3.17} \right)^{\frac{\mu+2}{236\mu}}. \quad (16)$$

For similar-sized complex craters on the Moon and Mercury (equal in D), assuming μ is the same on the Moon and Mercury and the only variable is surface gravity, ejecta from the same launch position (r) have the following ejection velocity ratio on Mercury and the Moon:

$$\frac{v_e(D)_M}{v_e(D)_L} = 1.49 * (0.909)^{\frac{\mu+2}{236\mu}}. \quad (17)$$

When $\mu = 0.41–0.55$ in Eq. (17) (Table A2), we obtain:

$$\frac{v_e(D)_M}{v_e(D)_L} = 1.18–1.24. \quad (18)$$

The result in Eq. (18) suggests that when only a difference in surface gravity is considered, craters on Mercury produce larger ejection velocities than similar-sized lunar craters. Inserting the value from Eq. (18) into Eq. (14), the ratio of the horizontal trajectory distances (R_e) can be calculated (Eq. (19)):

$$\frac{R_e^M}{R_e^L} = \left(\frac{v_e(D)_M}{v_e(D)_L} \right)^2 * \frac{g_L}{g_M} = 0.60–0.67. \quad (19)$$

Theoretically, this value is uniform for ejecta with the same launch positions (r). As previously noted, craters on Mercury may have smaller launch areas in the excavation cavity than same-sized lunar craters, so that ejecta with the same launch positions (r) on Mercury should always have smaller trajectory distances (Eq.

(19)). If assuming that the transition from continuous ejecta deposits to continuous secondaries facies occurs at the same ejection velocities for both lunar and mercurian craters, the gravity-regime crater scaling laws predict that mercurian craters have smaller continuous ejecta deposits and continuous secondaries facies than similar-sized lunar craters. Our observations in Figs. 3 and 4 verify this theoretical result (see also Eqs. (3) and (4)). Additionally, Abedin has a larger spatial density of secondaries than Copernicus and this observation can also be explained by the smaller continuous secondaries facies of Abedin due to the larger surface gravity on Mercury.

The larger surface gravity on Mercury can also explain the larger secondaries on Mercury than those of similar-sized lunar craters (Eq. (5)). Surface gravity and ejection velocity are two compensating variables in controlling the size of secondaries (e.g., Murray et al., 1974). Using the strength-regime crater scaling laws, volumes of transient craters of secondaries (V_s) are defined in Eq. (20) (Holsapple and Schmidt, 1987; Holsapple, 1993):

$$V_s = K_1 \left(\frac{m_e}{\rho_t} \right) \left(\frac{Y}{\rho_t v_e^2} \right)^{\frac{3\mu}{2}}. \quad (20)$$

m_e is the mass of the ejecta and v_e is the ejection velocity of the ejecta. Ideally, if the ejecta forming the largest secondaries on the Moon and Mercury have the same masses (m_e) and material properties (Y and μ ; Table A2 in the appendix), then Eqs. (7), (8), (9), and (20) predict that the ratio for the size of the largest secondaries between Mercury and the Moon ($\frac{d^M}{d^L}$) is only related with the ratio of the ejection velocity ($\frac{v_e^M}{v_e^L}$):

$$\frac{d^M}{d^L} = \left(\frac{v_e^M}{v_e^L} \right)^\mu. \quad (21)$$

The ejection velocity ratio predicted by the gravity-regime crater scaling laws (Eq. (18)) would yield a diameter ratio of secondaries ($\frac{d^M}{d^L}$) of ~ 1.35 , which is within the ratio range of $\sim 1\text{--}2$ of our observation (Eq. (5)).

In general, our observations reflect the contribution of Mercury's 2.3 times larger surface gravity than the Moon to the impact excavation process. The theoretical results predicted from the gravity-regime crater scaling (Eq. (19)) laws are consistent with both the results of Gault et al. (1975) and the arguments of many others about the significance of the larger surface gravity on Mercury on impact cratering (e.g., Murray et al., 1974; Guest and O'Donnell, 1977; Pike, 1980; Schultz and Singer, 1980; Melosh, 1989).

In contrast to the theoretical result shown in Eq. (19) that has only considered a difference of gravity on the excavation stage, our observed ratio for the radial extents of continuous ejecta deposits is 0.60–0.84 (Eq. (3)), and the observed ratio for the radial extents of continuous secondaries facies is 0.61–0.76 (Eq. (4)). This means that some craters on Mercury can form larger ejecta deposits ($L1$ and $L1 + L2$; Eqs. (3), (4)) than what is theoretically predicted and what was found in previous studies (e.g., Gault et al., 1975). These observations are not expected when only considering the effect of gravity on the impact excavation process (Eq. (19)).

Potential reasons for this difference include that (1) gravity may not be the only controlling factor in the impact excavation stage of forming complex craters on the Moon or Mercury, some other factors might also be important in this stage and form even larger ejection velocities and thus larger areas of ejecta deposits (see Sections 4.3 and 4.4); and/or that (2) the extents of continuous ejecta deposits and continuous secondaries facies of fresh complex craters on both the Moon and Mercury are not solely determined by their ballistic ranges.

The extent of ejecta deposits is not solely determined by trajectories of the ejecta. The theoretical trajectory distances (R_e) of impact ejecta shown in Eq. (19) are from their launch positions to the landing sites (Fig. 1). On the contrary, the values of $L1$ and $L1 + L2$ in this study (Eqs. (3) and (4)) are from crater rims to the outmost of continuous ejecta deposits and continuous secondaries facies, respectively. Following the cessation of the impact excavation stage, the transient crater collapses due to the over-steepened crater wall and/or dynamic rebounding of the crater floor (Melosh and Ivanov, 1999). The collapse will cause $L1$ and $L1 + L2$ smaller than the actual ballistic ranges of the ejecta (R_e). The collapse of transient craters is mainly affected by surface gravity (Melosh and Ivanov, 1999), and the prediction made from the empirical relationship between transient and final crater diameters (Eq. (15)) suggests that mercurian craters endured greater crater collapse after the excavation stage compared with same-sized (D) lunar craters. Therefore, taking account the effect of the greater collapse on Mercury would indicate that the ratios of both $L1$ and $L1 + L2$ between same-sized mercurian and lunar craters (Eqs. (3) and (4)) are smaller than those of the actual ballistic ranges (Eq. (19)), which is contrary to our observations in Eqs. (3) and (4).

Landing of ejecta would cause lateral ballistic sedimentation due to the horizontal component of the ejection velocity. Ballistic sedimentation has been known to be important in the deposition of impact ejecta on the Moon (e.g., Oberbeck, 1975; Melosh, 1989). For example, radial ridges in continuous ejecta deposits of lunar craters may represent the interaction of secondary cratering and lateral flows caused by ballistic sedimentation (Oberbeck, 1975). This process would enlarge the original extent of ejecta deposits (especially for continuous ejecta deposits), making the observed radial extent of ejecta deposits (e.g., $L1$ and $L1 + L2$) larger than expected. Ballistic sedimentation would be more obvious on Mercury because the gravity-regime crater scaling laws predict that mercurian craters form averagely larger ejection velocities than similar-sized lunar craters (Eq. (18)).

In our observation, some mercurian craters can form larger extents of continuous ejecta deposits and continuous secondaries facies than theoretically predicted using the gravity-regime crater scaling laws (Eq. (19) vs Eqs. (3) and (4)). Considering the opposite effect of ballistic sedimentation and crater collapse on the extent of ejecta deposits, a plausible interpretation for this observation is that ballistic sedimentation may be more significant than crater collapse in affecting the size of ejecta deposits on Mercury due to the larger ejection velocity formed during the impact excavation stage.

4.3. The effect of impact velocity on impact excavation processes

Projectiles striking Mercury have a larger median impact velocity (42.5 km/s) than those on the Moon (19.4 km/s; Le Feuvre and Wieczorek, 2008). Also, Mercury has a large span of impact velocities ranging from $\sim 18\text{--}135$ km/s (Minton and Malhotra, 2010). Physical simulations of impact cratering show that a larger impact velocity results in larger ejection velocities (e.g., Hermalyn and Schultz, 2010).

Following the gravity-regime crater scaling laws for lunar and mercurian complex craters (Eqs. (6)–(11)), ejection velocity is affected by numerous factors as shown in the following equation.

$$v_e(v_i) = \frac{\sqrt{2}}{C_{Tg}} \frac{\mu}{\mu + 1} \sqrt{g} r^{-\frac{1}{\mu}} \left(4K_1 a^3 \left(\frac{\rho_i}{\rho_t} \right)^{\frac{2}{2+\mu}} \left(\frac{ga}{v_i^2} \right)^{-\frac{3\mu}{2+\mu}} \right)^{\frac{1}{3}}. \quad (22)$$

We see that v_e increases with larger v_i when ignoring the other variables, i.e., sizes of projectile (a) and material properties (both target and ejecta). However, in this case, the diameter of the parent crater (D) is not necessarily constant because D is affected by both impact

velocity and target/projectile properties (Eq. (6)). Indeed, with the gravity-regime crater scaling laws, it is not empirically possible to separate material properties and impact velocity to evaluate their individual contribution to ejection velocity on the premise of the same diameter (Eq. (16)).

Here we argue that for same-sized craters, a larger impact velocity producing larger ejection velocities is demonstrated from the comparison of Abedin and Hokusai. Hokusai is one of the most prominent impact structures on Mercury that have sharp impact rays. The rays are unique because they are more than 4500 km long and extend across the whole northern hemisphere. Abedin is also a Class 1 crater that is located on the northern volcanic plains (Head et al., 2011) and it has a similar diameter to that of Hokusai. Hokusai has a proto-central peak ring on its floor but Abedin does not (Figs. 7a and b). If peak rings of impact basins are formed by collapse of nested impact melt (cf. Head, 2010; Baker et al., 2011), more impact melt may have produced by the Hokusai impact indicating it may have a larger impact velocity (Cintala, 1992; Cintala and Grieve, 1998). On the other hand, the continuous secondaries facies of Hokusai and Abedin are almost the same size (S2; Table A1), indicating the ejecta forming this facies of the two craters have comparable ejection velocities. However, the density of Hokusai's secondaries is about three to eight times smaller than that of Abedin (Fig. 8c). This observation suggests that fewer secondaries form on the continuous secondaries facies of Hokusai than Abedin. A possible reason is that due to the potentially larger impactor velocity of Hokusai than that of Abedin, ejecta that have same launch positions (r) in the excavation cavity of Hokusai may have greater ejection velocities. Therefore, Hokusai's ejecta are launched farther to form the distinctively long impact rays and fewer ejecta from Hokusai had the appropriate ejection velocities to form the continuous secondaries facies. Hokusai also has a smaller crater density of secondaries on the continuous secondaries facies than the similar-sized Copernicus crater on the Moon. This observation appears to be consistent with the assumption that the larger impact velocity of Hokusai had caused larger ejection velocities. However, it is not clear whether or not the larger median impact velocity on Mercury also causes greater ejection velocities compared with similar-sized lunar craters. If it was true, the additional larger ejection velocities contributed by impactor velocity would explain that some mercurian craters can form both larger extents of ejecta deposits (Eqs. (3) and (4)) and bigger secondaries (Eq. (5)) than theoretically predicted (Eqs. (19) and (21)).

In summary, impacts on Mercury produce larger ejection velocities than similar-sized lunar craters as shown in the gravity-regime crater scaling laws (Eq. (18)). Considering the combined effect of crater collapse and ballistic sedimentation caused by landing of ejecta, most of our observations are consistent with the gravity-regime crater scaling laws, indicating that gravity is a major controlling factor in the excavation stage of complex impact craters on both the Moon and Mercury. On the other hand, although it is not proved in the gravity-regime crater scaling laws that the larger median impact velocity on Mercury might also facilitate larger ejection velocities, the large span of impact velocities on Mercury may cause different ejection velocities for similar-sized craters on this planet, which give rise to the different spatial densities of secondaries for similar-sized craters, e.g., those of Abedin and Hokusai. This observation suggests that impact velocity may also affect the impact excavation stage, but its importance is not that obvious compared with gravity when comparing lunar and mercurian complex craters.

4.4. The effect of target properties on impact excavation processes

Gault et al. (1975) found that the herringbone pattern and V-shaped morphology frequently associated with lunar secondaries

are generally not found on Mercury. They attributed this to the limited resolution of Mariner 10 images (1 km/pixel on average). However, the herringbone morphology of lunar secondaries is visible at low Earth-based telescopic resolutions (Oberbeck and Morrison, 1973) whereas circular secondaries on Mercury are obvious at resolutions as good as 250 m/pixel (Fig. 5). Therefore, image resolution may not be a main reason for the more circular secondaries on Mercury.

On airless bodies, the morphology of secondaries is affected by both ejection velocity and angle. Schaber and Boyce (1976) and Scott (1977) found that secondaries on Mercury are better preserved than those on the Moon around primary craters of similar size and morphology. They suggested the larger ejection velocity on Mercury could cause this difference, because ejection velocities on Mercury are about 50% greater than on the Moon for an equivalent ejection range. Higher ejection velocities may produce morphologically enhanced secondary craters that, when ignoring the larger surface erosion rate on Mercury (Cintala, 1992), may account for the better preservation of secondaries with time (Schultz, 1988). However, many fresh craters on Mercury also have irregularly-shaped secondaries similar to their lunar counterparts (e.g., Fig. 6d), although the ejection velocities on Mercury are generally larger. This observation suggests that neither the larger median impact velocity nor the larger surface gravity on Mercury, or their combined effect, could cause the more circular secondaries around some mercurian craters. The most likely reason for the more circular secondaries on Mercury is that larger ejection angles were produced during the impact excavation process.

When the ejection velocities are the same, a larger ejection angle forms more circular secondaries (e.g., Oberbeck and Morrison, 1973). By experimental impact simulations, Gault and Greeley (1978) and Greeley et al. (1980) found that impacts in volatile-rich targets had appreciably higher ejection angles than those in depleted targets. Thomsen et al. (1979, 1980) and Greeley et al. (1982) confirmed this observation. Recent numerical modeling of impacts in ice-rock mixture found that the initial ejection angles in such impacts can be as large as 70° due to the effect of subsurface volatiles (cf. Stewart et al., 2001). Schultz and Singer (1980) found that some martian craters have more circular secondaries than lunar craters. They referred to earlier finding that the existence of subsurface ice at the pre-impact sites on Mars provided a lower strength target and hence produced larger ejection angles. Schaber et al. (1977) suggested that the crustal viscosity of very early Mercury could have been less than that of the Moon because higher subsurface temperatures may have existed at that time. They also suggested that the present viscosity of the mercurian surface is greater than that in the past. However, no quantitative constraints have yet been established for the relationship between target viscosity and ejection angle.

Mercury was formerly considered to be a planet depleted of crustal volatiles, similar to the Moon (Lewis, 1972; Murray et al., 1975; Schultz, 1988). MESSENGER found that Mercury's surface exhibits morphological evidence for widespread volatile-related activity (Blewett et al., 2011, 2012; Xiao et al., 2013a), and the spectrometers onboard of MESSENGER have found higher abundances of crustal volatile elements (e.g., Na, K, S) than were predicted by high-temperature formation scenarios for Mercury (cf. Peplowski et al., 2011, 2012; Nittler et al., 2011; Weider et al., 2012). However, the total amount of crustal volatiles on Mercury is still significantly lower than that on Mars or on the outer Solar System icy satellites. Xiao and Komatsu (2013) and Xiao et al. (2014) found that some craters on the Moon and Mercury have layered ejecta flows and/or central pits that are morphologically similar with those on Mars and outer Solar System icy satellites. They suggested that the relatively low content of crustal volatiles on the Moon and Mercury is not adequate to form the ejecta flows or the

central pits, which is consistent with previous findings (Schultz, 1988).

We noticed that hollows (Blewett et al., 2011, 2012) and dark spots (Xiao et al., 2013a), which may indicate a high concentration of crustal volatiles at the pre-impact surfaces, occur in some of the observed mercurian craters that have circular secondaries. For examples, Atget (Fig. 5d; Xiao et al., 2013a) and Tyagaraja (Fig. 5h; Blewett et al., 2011, 2012) have dark spots and/or hollows on the crater floors. More commonly, mercurian craters that have circular secondaries are usually associated with excavated low-reflectance material (cf. Robinson et al., 2008; Denevi et al., 2009), which represents a distinct target material on Mercury (Nittler et al., 2011; Weider et al., 2012). For example, Tyagaraja (Fig. 5d; Blewett et al., 2011, 2012), Rachmaninoff (Fig. 6a; Prockter et al., 2010), Raditaladi (Fig. 6b; Prockter et al., 2010), and Mozart (Fig. 6c; Xiao et al., 2013a) all have surrounding low-reflectance material on the continuous ejecta deposits, indicating these impacts have excavated subsurface material that has different spectral properties. The low-reflectance material is not a homogeneous unit on Mercury and it has a higher content of sulfur compared to the rest of the planet (e.g., Nittler et al., 2011). However, its physical properties are not fully known. Whether or not the low-reflectance material and/or the limited crustal volatiles on Mercury have caused larger ejection angles during the impact excavation process, therefore producing the observed circular secondaries is not clear. Without further compositional information, we cannot provide conclusive constraints on the properties of the crustal volatiles or the low-reflectance material on Mercury, or their potential effect on the excavation process.

On the Moon, we find that very few craters or basins have similar circular and isolated secondaries on the continuous secondaries deposits, e.g., the Orientale basin and the Antoniadi crater (Fig. 5i–l). However, it is not clear whether or not crustal and/or mantle material of different properties was excavated by these impacts compared to the other craters or basins on the Moon (e.g., Belton et al., 1992; Head et al., 1993). Therefore, these exceptions on the Moon need to be further investigated.

4.5. Problems remaining

In our analysis, we interpret that the more circular secondaries on Mercury are caused by larger ejection angles. It should be noted that larger ejection angles also affect the size of secondaries because only the vertical component of the impactor's kinetic energy and momentum determine the size of secondaries (e.g., Gault and Wedekind, 1978; Elbeshausen et al., 2007). The size of continuous ejecta deposits and continuous secondaries facies are also affected by ejection angles (Eqs. (12) and (13)) because ejection angles larger or smaller than 45° produce different-sized ballistic distances and amount of lateral flows when the ejection velocity is the same. In this study, the effects of target properties on the sizes of d_{max} , S1 and S2 were not considered. Also, the location, stratigraphic age, and size distribution of craters having circular and isolated secondaries on Mercury have not yet been fully determined. If temporal and spatial variations of target properties affect the size, shape and frequency of secondaries, they need to be accounted for.

Impact angles may severely affect the energy partitioning during the impact process and thus form an asymmetric distribution of impact rays and ejecta deposits (e.g., Gault and Wedekind, 1978; Pierazzo and Melosh, 1999). The effect of the impact angle is important when studying the excavation stage of single craters (e.g., Schultz, 1992; Anderson et al., 2003; Schultz et al., 2007).

Here we normalized the incidence angle as 90° to emphasize the contribution of impact velocity.

5. Conclusions

Impact cratering is a complicated geological process controlled by numerous factors. We have investigated the effects of the three main factors thought responsible to govern the geometrical properties of ejecta facies exterior to craters during the impact excavation stage, namely impact velocity, surface gravity, and target material properties. Orbital images from MESSENGER reveal great differences in these exterior structures of similarly sized craters on the Moon and Mercury. We find that the surface areas of the continuous ejecta deposits and continuous secondaries facies are smaller for craters on Mercury than similar-sized lunar craters. This confirms previous findings and attests to the importance of surface gravity in affecting the surface area of ejecta deposit facies. In addition, the largest secondaries on the continuous secondaries facies of craters on Mercury are larger than those of similar-sized lunar craters on average. These results are largely consistent with predictions made from gravity-regime crater scaling laws, supporting that gravity is a major controlling factors in the excavation stage of forming complex impact craters on the Moon and Mercury.

We also find that the size ratios of continuous ejecta deposits and continuous secondaries facies between similar-sized craters on Mercury and the Moon are larger than both previous findings and predictions based on gravity-regime crater scaling laws. A possible interpretation is that mercurian complex craters form larger ejection velocities than similar-sized lunar craters during the gravity-controlled excavation stage, so that landing of ejecta on Mercury causes greater ballistic sedimentation and lateral flows. Furthermore, similar-sized craters on Mercury (e.g., Abedin and Hokusai) have different spatial densities of secondaries on their continuous secondaries facies, which may be caused by the large span of impact velocities on Mercury because the larger impact velocity of Hokusai may also induce greater ejection velocities during the excavation stage. However, the contribution of the different median impact velocity on the Moon and Mercury to ejection velocities is not clear.

Moreover, some, but not all craters on Mercury form more circular and isolated secondary craters on the continuous secondaries facies as compared to similar-sized lunar craters. The increased circularity of secondary craters on Mercury is not caused by the larger surface gravity or ejection velocity. Larger ejection angles must have formed during the impact excavation stage for these craters on Mercury. A probable reason is that these craters might spatially correspond to regions hosting geological units of different material properties compared to other portions of Mercury and those on the Moon.

Results of our study confirm previous findings that surface gravity is a dominant factor during the impact excavation stage governing the spatial extent of ejecta deposits. Also, gravity cannot be considered by itself because it is closely intertwined with other parameters, such as impact velocity and target properties, in affecting the impact excavation stage. While surface gravity can be considered relatively constant throughout a planetary body, impact velocity and target materials may have a large range of variability. We have shown a few exemplary comparative analyses of craters on Mercury to highlight the effect of these variabilities on impact cratering on the same planetary body. Therefore, we conclude that gravity is a major controlling factor on the impact excavation stage of the formation of complex impact craters on the Moon and Mercury. Impact velocity and properties of target material may also play an important, but relatively minor, role in the impact excavation stage.

Acknowledgments

We appreciate the constructive comments from James E. Richardson Jr. and an anonymous reviewer, which have greatly improved the manuscript. We thank David T. Blewett, Maria E. Banks, and Caleb I. Fassett for a careful reading and critique of the paper. The MESSENGER project is supported by the NASA Discovery Program under contracts NAS5-97271 (to the Johns Hopkins University Applied Physics Laboratory) and NASW-00002 (to the Department of Terrestrial Magnetism, Carnegie Institution of Washington). Z.X. thanks the constant encouragement from Professor Zuoxun Zeng.

Appendix A. Supplementary material

Supplementary data associated with this article can be found, in the online version, at <http://dx.doi.org/10.1016/j.icarus.2013.10.002>.

References

- Anderson, J.L.B., Schultz, P.H., Heineck, J.T., 2003. Asymmetry of ejecta flow during oblique impacts using three-dimensional particle image velocimetry. *J. Geophys. Res.* 108, 5094. <http://dx.doi.org/10.1029/2003JE002075>.
- Anderson, J.L.B., Schultz, P.H., Heineck, J.T., 2004. Experimental ejection angles for oblique impacts: Implications for the subsurface flow-field. *Meteorit. Planet. Sci.* 39, 303–320.
- Arthur, D.W.G., Agniray, A.P., Howath, R.A., Wood, C.A., Chapman, C.R., 1963. The system of lunar craters. *Commun. Lunar Planet. Lab.* 2, 71–78.
- Arvidson, R.E. et al., 1979. Standard techniques for presentation and analysis of crater size-frequency data. *Icarus* 37, 467–474. [http://dx.doi.org/10.1016/0019-1035\(79\)90009-5](http://dx.doi.org/10.1016/0019-1035(79)90009-5).
- Baker, D.M.H. et al., 2011. The transition from complex crater to peak-ring basin on Mercury: New observations from MESSENGER flyby data and constraints on basin formation models. *Planet. Space Sci.* 15, 1932–1948. <http://dx.doi.org/10.1016/j.pss.2011.05.010>.
- Belton, M.J.S. et al., 1992. Lunar impact basins and crustal heterogeneity: New western limb and farside data from Galileo. *Science* 255, 570–576.
- Blewett, D.T. et al., 2011. Hollows on Mercury: MESSENGER evidence for geologically recent volatile-related activity. *Science* 333, 1856–1859.
- Blewett, D.T. et al., 2012. Mercury's hollows: Constraints on formation and composition from analysis of geological setting and spectral reflectance. *J. Geophys. Res.* 118, 1013–1032. <http://dx.doi.org/10.1029/2012JE004174>.
- Buckingham, E., 1914. On physically similar systems: Illustrations of the use of dimensional equations. *Phys. Rev.* 4 (4), 345–376.
- Cintala, M.J., 1992. Impact-induced thermal effects in the lunar and mercurian regoliths. *J. Geophys. Res.* 97 (E1), 947–973. <http://dx.doi.org/10.1029/91JE02207>.
- Cintala, M.J., Grieve, R.A.F., 1998. Scaling impact-melt and crater dimensions: Implications for the lunar cratering record. *Meteorit. Planet. Sci.* 33, 889–912. <http://dx.doi.org/10.1111/j.1945-5100.1998.tb01695.x>.
- Cintala, M.J., Head, J.W., Mutch, T.A., 1976. Characteristic of martian craters as a function of diameter: Comparison with the Moon and Mercury. *Geophys. Res. Lett.* 3, 117–120.
- Cintala, M.J., Wood, C.A., Head, J.W., 1977. The effects of target characteristics on fresh impact crater morphologic features: Preliminary results for the Moon and Mercury. *Proc. Lunar Sci. Conf.* 8, 3409–3425.
- Croft, S.K., 1980. Cratering flow fields: Implications for the excavation and transient expansion stages of crater formation. *Proc. Lunar Planet. Sci. Conf.* 11, 2347–2378.
- Croft, S.K., 1985. The scaling of complex craters: Proceedings of the 15th Lunar and Planetary Science Conference. *J. Geophys. Res.* 90, C828–C842.
- Denevi, B.W. et al., 2009. The evolution of Mercury's crust: A global perspective from MESSENGER. *Science* 324, 613–618. <http://dx.doi.org/10.1126/science.1172226>.
- Elbeshausen, D., Wünnemann, K., Collins, G.S., 2007. Three-dimensional numerical modeling of oblique impact processes: Scaling of cratering efficiency. *Lunar Planet. Sci.* 38, Abstract 1952.
- Gault, D.E., Greeley, R., 1978. Exploratory experiments of impact craters formed in viscous-liquid targets: Analogs for martian rampart craters? *Icarus* 34, 486–495. [http://dx.doi.org/10.1016/0019-1035\(78\)90040-4](http://dx.doi.org/10.1016/0019-1035(78)90040-4).
- Gault, D.E., Wedekind, J.A., 1978. Experimental studies of oblique impact. *Lunar Planet. Sci.* 9, 374–376.
- Gault, D.E., Quaide, W.L., Oberbeck, V.R., 1968. Impact cratering mechanics and structure. In: French, B.M., Short, N.M. (Eds.), *Shock Metamorphism of Natural Materials*. Mono Book Corporation, pp. 87–99.
- Gault, D.E., Gust, J.E., Murry, J.B., Dzurisin, D., Malin, M.C., 1975. Some comparisons of impact craters on Mercury and the Moon. *Geophys. Res. Lett.* 80 (17), 2444–2460.
- Greeley, R., Fink, J., Gault, D.E., Snyder, D.B., Guest, J.E., Schultz, P.H., 1980. Impact cratering in viscous targets: Laboratory experiments. *Proc. Lunar Sci. Conf.* 11, 2075–2097.
- Greeley, R., Fink, J., Gault, D.E., Guest, J.E., 1982. Experimental simulation of impact cratering on icy satellites. In: Morrison, D. (Ed.), *Satellites of Jupiter*. University of Arizona Press, Tucson, pp. 340–378.
- Guest, J.E., O'Donnell, W.P., 1977. Surface history of Mercury: A review. *Vistas Astron.* 20, 273–300.
- Hawkins, S.E. et al., 2007. The Mercury dual imaging system on the MESSENGER spacecraft. *Space Sci. Rev.* 131, 247–338.
- Head III J.W., 1976. The significance of substrate characteristics in determining morphology and morphometry of lunar craters. *Proc. Lunar Sci. Conf.* 7, 2913–2929.
- Head III, J.W., 2010. Transition from complex craters to multi-ringed basins on terrestrial planetary bodies: Scale-dependent role of the expanding melt cavity and progressive interaction with the displaced zone. *Geophys. Res. Lett.* 37, L02203. <http://dx.doi.org/10.1029/2009GL041790>.
- Head III, J.W. et al., 1993. Lunar impact basins: New data for the western limb and far side (Orientale and South Pole-Aitken basins) from the first Galileo flyby. *J. Geophys. Res.* 98, 17149–17181.
- Head III, J.W. et al., 2010. Global distribution of large lunar craters: Implications for resurfacing and impactor populations. *Science* 329, 1504–1507.
- Head III, J.W. et al., 2011. Flood volcanism in the northern high latitudes of Mercury revealed by MESSENGER. *Science* 333, 1853–1856. <http://dx.doi.org/10.1126/science.1211997>.
- Hermalyn, B., Schultz, P.H., 2010. Early-stage ejecta velocity distribution for vertical hypervelocity impacts into sand. *Icarus* 209, 866–870.
- Holsapple, K.A., 1993. The scaling of impact processes in planetary sciences. *Annu. Rev. Earth Planet. Sci.* 21, 333–373.
- Holsapple, K.A., Schmidt, R.M., 1979. A material-strength model for apparent crater volume. *Proc. Lunar Sci. Conf.* 10, 2757–2777.
- Holsapple, K.A., Schmidt, R.M., 1987. Point source solutions and coupling parameters in cratering mechanics. *J. Geophys. Res.* 92, 6350–6376.
- Housen, K.R., Schmidt, R.M., Holsapple, K.A., 1983. Crater ejecta scaling laws: Fundamental forms based on dimensional analysis. *J. Geophys. Res.* 88 (B3), 2485–2499. <http://dx.doi.org/10.1029/JB088iB03p02485>.
- Le Feuvre, M.L., Wieczorek, M.A., 2008. Nonuniform cratering of the terrestrial planets. *Icarus* 197, 291–306. <http://dx.doi.org/10.1016/j.icarus.2008.04.011>.
- Lewis, J.S., 1972. Metal/silicate fractionation in the Solar System. *Earth Planet. Sci. Lett.* 15, 286–290.
- Malin, M.C., Dzurisin, D., 1978. Modification of fresh crater landforms: Evidence from the Moon and Mercury. *J. Geophys. Res.* 83, 233–243.
- Maxwell, D.E., 1977. Simple Z model for cratering, ejection, and the overturned flap. In: Roddy, D.J., Pepin, R.O., Merrill, R.B. (Eds.), *Impact and Explosion Cratering: Planetary and Terrestrial Implications*. Pergamon, New York, pp. 1003–1008.
- Maxwell, D., Seifert, K., 1974. Modeling of cratering, close-in displacements, and ejecta. Report DNA 3628F, Defense Nuclear Agency, Washington, DC.
- Melosh, H.J., 1989. *Impact Cratering: A Geologic Process*. Oxford University Press, New York, pp. 1–255.
- Melosh, H.J., Ivanov, B.A., 1999. Impact crater collapse. *Annu. Rev. Earth Planet. Sci.* 27, 385–415.
- Minton, D.A., Malhotra, R., 2010. Dynamical erosion of the asteroid belt and implications for large impacts in the inner Solar System. *Icarus* 207, 744–757. <http://dx.doi.org/10.1016/j.icarus.2009.12.008>.
- Murchie, S.L. et al., 2008. Geology of the Caloris basin, Mercury: A view from MESSENGER. *Science* 321, 73–76.
- Murray, B.C. et al., 1974. Mercury's surface: Preliminary description and interpretation from Mariner 10 pictures. *Science* 185 (4146), 169–179.
- Murray, B.C., Strom, R.G., Trask, N.J., Gault, D.E., 1975. Surface history of Mercury: Implications for terrestrial planets. *J. Geophys. Res.* 80, 2508–2514.
- Nittler, L.R. et al., 2011. The major-element composition of Mercury's surface from MESSENGER X-ray spectrometry. *Science* 333, 1847–1850.
- Oberbeck, V.R., 1975. The role of ballistic erosion and sedimentation in lunar stratigraphy. *Rev. Geophys.* 13 (2), 337–362. <http://dx.doi.org/10.1029/RG013i002p00337>.
- Oberbeck, V.R., Morrison, R.A., 1973. The lunar herringbone pattern. *NASA Spec. Publ.* 330, Section 32, pp. 15–29.
- Oberbeck, V.R., Morrison, R.H., 1974. Laboratory simulation of the herringbone pattern associated with lunar secondary crater chains. *Moon* 9, 415–455. <http://dx.doi.org/10.1007/BF00562581>.
- Oberbeck, V.R., Quaide, W.L., Arvidson, R.E., Aggarwal, H.R., 1977. Comparative studies of lunar, martian, and mercurian craters and plains. *J. Geophys. Res.* 82, 1681–1698.
- Ostrach, L.R., Robinson, M.S., Denevi, B.W., Thomas, P.C., 2011. Effects of incidence angle on crater counting observations. *Lunar Planet. Sci.* 42, Abstract 1202.
- Ostrach, L.R., Robinson, M.S., Denevi, B.W., 2012. Distribution of impact melt on Mercury and the Moon. *Lunar Planet. Sci.* 43, Abstract 1113.
- Pepłowski, R.N. et al., 2011. Radioactive elements on Mercury's surface from MESSENGER: Implications for the planet's formation and evolution. *Science* 333, 1850–1852.

- Peplowski, P.N. et al., 2012. Variations in the abundances of potassium and thorium on the surface of Mercury: Results from the MESSENGER Gamma-Ray Spectrometer. *J. Geophys. Res.* 117, E00L04. <http://dx.doi.org/10.1029/2012JE004141>.
- Pierazzo, Z., Melosh, H.J., 1999. Hydrocode modeling of Chicxulub as an oblique impact event. *Earth Planet. Sci. Lett.* 165 (2), 163–176.
- Pike, R.J., 1977. Size-dependence in the shape of fresh impact craters on the Moon. In: Impact and Explosion Cratering: Planetary and Terrestrial Implications. Proceedings of the Symposium on Planetary Cratering Mechanics, Flagstaff, Arizona, pp. 489–509.
- Pike, R.J., 1980. Control of crater morphology by gravity and target type: Mars, Earth, Moon. *Proc. Lunar Sci. Conf.* 11, 2159–2189.
- Pike, R.J., 1988. *Geomorphology of impact craters on Mercury*. In: Vilas, F., Chapman, C.R., Matthews, M.S. (Eds.), *Mercury*. University of Arizona Press, Tucson, Arizona, pp. 165–273.
- Prockter, L.M. et al., 2010. Evidence for young volcanism on Mercury from the third MESSENGER flyby. *Science* 329, 668–671. <http://dx.doi.org/10.1126/science.1188186>.
- Richardson, J.E., Melosh, H.J., Lisse, C.M., Carcich, B., 2007. A ballistics analysis of the Deep Impact ejecta plume: Determining Comet Tempel 1's gravity, mass, and density. *Icarus* 190, 357–390. <http://dx.doi.org/10.1016/j.icarus.2007.08.033>.
- Robinson, M.S. et al., 2008. Reflectance and color variations on Mercury: Regolith processes and compositional heterogeneity. *Science* 321, 66–69. <http://dx.doi.org/10.1126/science.1160080>.
- Robinson, M.S. et al., 2010. *Lunar Reconnaissance Orbiter Camera (LROC) instrument overview*. *Space Sci. Rev.* 150 (1–4), 81–124.
- Schaber, G.G., Boyce, J.M., 1976. Moon–Mercury: Basins, secondary craters and early flux history. In: Conf.: Comparisons of Mercury and the Moon LSI Contrib. 262, p. 28.
- Schaber, G.G., Boyce, J.M., Trask, N.J., 1977. Moon–Mercury: Large impact structures, isostasy and average crustal viscosity. *Phys. Earth Planet. Int.* 15, 189–201.
- Schultz, P.H., 1976. *Moon Morphology*. University of Texas Press, Austin, Texas, pp. 1–604.
- Schultz, P.H., 1988. Cratering on Mercury: A relook. In: Vilas, F., Chapman, C.R., Matthews, M.S. (Eds.), *Mercury*. University of Arizona Press, Tucson, Arizona, pp. 274–335.
- Schultz, P.H., 1992. Atmospheric effects on ejecta emplacement and crater formation on Venus from Magellan. *J. Geophys. Res.* 97, 16183–16248.
- Schultz, P.H., Gault, D.E., 1985. Clustered impacts: Experiments and implications. *J. Geophys. Res.* 90, 3701–3732.
- Schultz, P.H., Singer, J., 1980. A comparison of secondary craters on the Moon, Mercury and Mars. *Proc. Lunar Sci. Conf.* 11, 2243–2259.
- Schultz, P.H., Eberhardt, C.A., Ernst, C.M., A'Hearn, M.F., Sunshine, J.M., Lisse, C.M., 2007. The Deep Impact oblique impact cratering experiment. *Icarus* 190, 295–333. <http://dx.doi.org/10.1016/j.icarus.2007.06.006>.
- Scott, D.H., 1977. Moon–Mercury: Relative preservation states of secondary craters. *Phys. Earth Planet. Int.* 15, 173–178.
- Shoemaker, E.M., 1965. Preliminary analysis of the fine structure of the lunar surface in Mare Cognitum. In: Ranger 7, Part 2, Experimenters' Analyses and Interpretations. JPL/NASA Technical Report, 32–700, pp. 75–134.
- Smith, E.I., Hartnell, J.A., 1978. Crater size-shape profiles for the Moon and Mercury: Terrace effects and interplanetary comparisons. *Moon Planets* 19, 479–511.
- Solomon, S.C. et al., 2001. The MESSENGER mission to Mercury: Scientific objectives and implementation. *Planet. Space Sci.* 49, 1445–1465.
- Stewart, S.T., O'Keefe, J.D., Ahrens, T.J., 2001. The relationship between rampart crater morphologies and the amount of subsurface ice. *Lunar Planet. Sci. XXXII. Abstract* 2092.
- Strom, R.G., 1979. Mercury: A post Mariner-10 assessment. *Space Sci. Rev.* 24, 3–70.
- Strom, R.G., Malhotra, R., Ito, T., Yoshida, F., Kring, D.A., 2005. The origin of planetary impactors in the inner Solar System. *Science* 309, 1847–1850. <http://dx.doi.org/10.1126/science.1113544>.
- Strom, R.G., Chapman, C.R., Merline, W.J., Solomon, S.C., Head, J.W., 2008. Mercury cratering record viewed from MESSENGER's first flyby. *Science* 321, 79–81. <http://dx.doi.org/10.1126/science.1159317>.
- Thomsen, J.M., Austin, M.G., Ruhl, S.F., Schultz, P.H., Orphal, D.L., 1979. Calculational investigation of impact cratering dynamics: Early time material motions. *Proc. Lunar Sci. Conf.* 10, 2741–2756.
- Thomsen, J.M., Austin, M.G., Schultz, P.H., 1980. The development of the ejecta plume in a laboratory-scale impact cratering events. *Lunar Planet. Sci.* 11. Abstract 1148.
- Trask, N.J., Guest, J.E., 1975. Preliminary geologic terrain map of Mercury. *J. Geophys. Res.* 80, 2462–2477.
- Weider, S.Z. et al., 2012. Chemical heterogeneity on Mercury's surface revealed by the MESSENGER X-Ray Spectrometer. *J. Geophys. Res.* 117, E00L05. <http://dx.doi.org/10.1029/2012JE004153>.
- Wilcox, B.B., Robinson, M.S., Thomas, P.C., Hawke, B.R., 2005. Constraints on the depth and variability of the lunar regolith. *Meteorit. Planet. Sci.* 40, 695–710. <http://dx.doi.org/10.1111/j.1945-5100.2005.tb00974.x>.
- Wood, C.A., Anderson, L., 1978. New morphometric data for fresh lunar craters. *Proc. Lunar Sci. Conf.* 9, 3669.
- Xiao, Z., Komatsu, G., 2013. Impact craters with ejecta flows and central pits on Mercury. *Planet. Space Sci.* 82, 62–78.
- Xiao, Z., Strom, R.G., 2012. Problems determining relative and absolute ages using the small crater population. *Icarus* 220, 254–267.
- Xiao, Z. et al., 2013a. Dark spots on Mercury: A hollow-related low-reflectance material. *J. Geophys. Res.* 118, 1752–1765.
- Xiao, Z., Zeng, Z., Komatsu, G., 2014. A global inventory of central pit craters on the Moon: Distribution, morphology, and geometry. *Icarus* 227, 195–201. <http://dx.doi.org/10.1016/j.icarus.2013.09.019>.